


Research paper

A description of plume-surface interactions and non-dimensional analysis for crater formation

Gregory S. Shallcross^{a,*}, Jason Rabinovitch^b ^a Jet Propulsion Laboratory, California Institute of Technology, 4800 Oak Grove Drive, Pasadena, 91109, CA, USA^b Stevens Institute of Technology, Hoboken, 07030, NJ, USA

ARTICLE INFO

Keywords:

Plume-surface interactions

Non-dimensional analysis

Particles

Erosion

ABSTRACT

During entry, descent, and landing, the exhaust plume from a spacecraft interacts with a satellite body or planetary surface. This phenomenon, commonly referred to as plume-surface interactions, can lead to spacecraft aerodynamic disturbances and induced heating, ejection of granular material, landing site obscuration, and crater formation. In this manuscript, a thorough review of theory, existing modeling frameworks, and available experimental data are described for crater formation. A method based on non-dimensional analysis and scaling is proposed, and scaling terms are determined using the Buckingham-Pi approach, including a new non-dimensional rate number describing the excavation of granular material. This approach is applied to experiments of round jet impingement on granular beds from available literature. This provides a framework to estimate crater size and shape for plume-surface interactions and can be improved as more data becomes available.

1. Introduction

During planetary descent, rocket engine exhaust impinges on a landing site resulting in a series of engineering challenges. Entrained material can obscure the ground-plane, spoof sensors, collide with the lander, and form significant craters [1,2]. This phenomenon, also known as plume-surface interactions (PSI), can significantly jeopardize mission safety and has been a known risk since the first lunar missions in the 1960's (example missions include the Surveyor and Apollo programs [3–5]). Even with decades of missions involving planetary landing, accurate predictions of crater growth remain challenging and elusive.

During landing, spacecraft structures, such as the landing gear, can interact with a crater generated via PSI, causing stability issues [6]. This problem is also present for other environmental erosion applications including, but not limited to, hydrology, civil, and transportation engineering [1,7,8]. Such examples typically occur over long timescales in the presence of flowing bodies of water under low-speed incompressible conditions. In stark contrast, the physics for spacecraft applications is a combination compressible flows, multiphase coupling, and large scale particle transport leading to rapid granular excavation [2,9,10]. As the rocket plume interacts with the surface, shock and regular flow structures form (see Fig. 1 for an example of under-expanded jet impingement). Under these conditions, a stagnation shock

is present along with a strong recirculation region. The recirculating flow rapidly entrains and ejects particles resulting in crater formation. During this process, shock-particle, particle-turbulence, and particle-particle interactions are observed, the physics of which are thoroughly discussed in Capecelatro [10] and Shallcross [2].

Many approaches are available to model the phenomenon with differing levels of fidelity and complexity to capture specific physical phenomena. These including high fidelity numerical multiphase flow methods [9–11], reduced-order physics based approximations [12,13], and empirical scaling [1,14,15]. High fidelity methods can be too computationally expensive and time intensive for engineering applications, while existing low fidelity methods are not validated against a wide range of operating conditions. In this work, a reduced-order approach is proposed to estimate crater formation. This starts with non-dimensional analysis for jet impingement on granular beds using the Buckingham-Pi procedure (Section 2.1). A model is proposed and demonstrated with a non-linear regression fitting procedure to extract modeling parameters from experimental data (Section 3.1), and regime specific phenomena are introduced (Section 3.2). Prior to discussions on modeling, a detailed description of the theory for PSI is provided. A recent review of experimental data and erosion mechanisms can be found in Cuesta et al. [16]. Here, we include a focused review of relevant mechanisms for our scaling work.

* Corresponding author.

E-mail address: gregory.s.shallcross@jpl.nasa.gov (G.S. Shallcross).

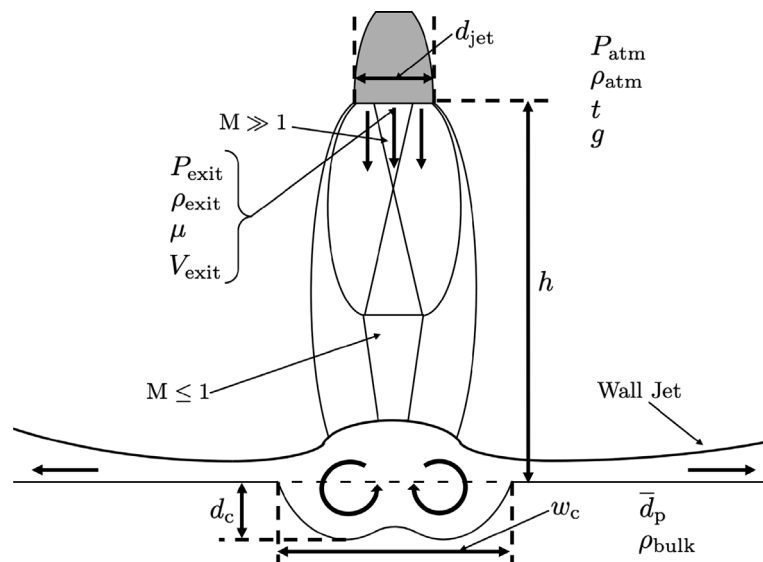


Fig. 1. Plume-surface interactions for under-expanded jet impingement on a granular surface at higher impingement heights.

1.1. Mechanisms of crater formation for plume-surface interactions

There are five mechanisms for crater formation that are commonly referred to in literature including: (1) viscous erosion, (2) bearing capacity failure, (3) diffusion-driven flow, (4) diffuse gas eruption, and (5) diffuse gas explosive erosion [17–19]. All mechanisms for granular erosion date back to the Apollo and Viking eras, apart from diffuse gas explosive erosion which is a special case for pulsed jet interactions with granular beds [17–19]. While descriptions of plume-surface interaction of the listed phenomena are included in other literature [18,19], they are briefly introduced here for completeness.

Viscous erosion occurs when shear stresses induce granular motion on a surface. This is usually captured through calculating the wall shear stress on a surface to see if it exceeds a critical shear stress criterion, sometimes defined by Mohr-Coloumb theory. Bearing capacity failure is the mechanism where the plume induced surface pressure and gravitational body forces of the material overcome the strength of the material during erosion. This leads to a structural failure and collapse of the material walls into a crater, thus inducing granular fluidization and ejecta formation. Diffusion-driven flow occurs when the induced flow environment pushes between granular interstitial sites. Here, the aerodynamic forces lead to bulk granular motion. Diffuse gas eruption occurs with induced pressure build up in the granular material. As pressure gradients grow and fluidization of particulate occurs, rapid excavation of material can occur. Diffuse gas explosive erosion occurs with the growth of large pore pressure, leading to rapid granular excavation.

The relative significance of the mechanisms and contributions to crater formation depends on the operating conditions. Under near-vacuum and/or rarefied environments a rocket plume expands, leading to a drop in impingement pressure while still achieving a large enough surface shear to displace granular media. These conditions are where viscous erosion is thought to dominate, resulting in an annular crater which exhibits a peak at the center of impingement with excavation in regions of high shear, see Fig. 2(a) for illustration purposes.

For environments with substantial atmosphere under continuum regimes, the rocket plume remains more columnated. This leads to higher induced pressures at the center of impingement and subsequent excavation of material through interactions of granular media with the energetic portion of the plume. Under these conditions, craters are shown to be parabolic in nature [15,18,20–22], see Fig. 2(b) for a representation of this shape.

While general crater types are observed for rarefied and continuum conditions, there are transitions between different shapes. For example under annular crater formation, collapse of the crater walls, shown in Fig. 2(a), can occur. This can modify the induced flow structures within the crater, allowing for the transition to parabolic crater formation, as shown in see Fig. 2(b). Similarly, a parabolic crater may grow to such a state that the sides of the crater collapse, resulting in nested paraboloids, or a double parabolic crater (see Fig. 2(c)) [15,18,20]. Even though different geometric shapes are observed under different operating conditions, the persistence and transitions between the behaviors have never been fully characterized.

1.2. Review of available plume-surface interaction data

The earliest PSI experiments date back to robotic spacecraft landing on the Moon (prior to the Apollo program landing humans on the Moon). The first set of lunar soft landings by the United States were the Surveyor missions, which occurred between 1966 and 1968 (though this was predated by the Luna Program from the Soviet Union [23]). Prior to these missions, experiments for hypersonic jet impingement on granular media for characterization of ejected mass flux from a surface were performed, which led to the development of Roberts model for surface shear induced erosion [12,13]. Throughout this era, experiments can be separated into two categories: (1) stationary jet impingement at fixed heights, and (2) descending jet impingement, where the nozzle descends to mimic landing [24]. Other atmospheric based studies involved solid rocket motor and cold gas test firings for descending and stationary jet configurations [25]. Direct observations were also collected during Apollo era from a camera mounted on Lunar Modules for video observations during landing [26]. This system was able to capture the first motion of granular material during descent and subsequent erosion and ejecta formation. While beneficial, the system was not designed to capture crater formation under the lander.

Additional experiments were collected for the Viking missions where robotic landers landed directly on the Martian surface. Due to the Martian environment, which has an expected surface pressure varying between 600–650 Pa, additional descending jet experiments were collected with a low back-pressure to replicate relevant environmental conditions [17,27,28]. The results of the experimental campaign eventually led to the development of the “shower-head engine” in attempt to mitigate the effects of plume-surface interactions. It was discovered that by increasing the number of engine nozzles, one can diffuse the rocket plume and drop the impingement pressure on a granular surface [29].

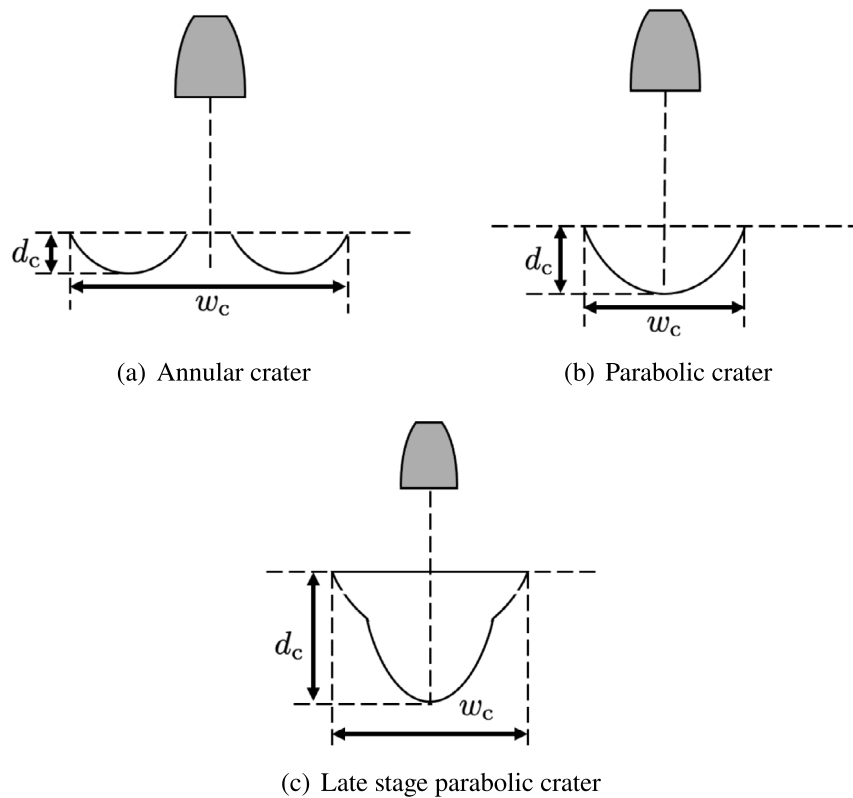


Fig. 2. Cross sections of different crater shapes for single jet impingement. This includes illustrations of (a) an annular crater in rarefied environments, (b) paraboloid craters in continuum early stage impingement, and (c) double paraboloid for later stage continuum impingement.

This information was used to develop requirements to ensure mission success, where the maximum crater depth and impingement pressures were limited to 5 cm and 2 kPa respectively [17,30].

Later landed missions to Mars used different technologies in an attempt to avoid or mitigate PSI hazards. Pathfinder [31] and Mars Exploration Rovers [32] used inflatable airbags to mitigate impact loads (instead of powered descent to the surface) to avoid crater formation during landing. Phoenix [33] and InSight [34,35] implemented pulsed engines for direct descent and landing. The Mars Science Laboratory [36] and Mars 2020 [37] missions used the Sky Crane procedure where a propulsion module lowered a payload keeping the rocket engines farther from the surface [38].

While these landing procedures attempted to mitigate effects of PSI, observations were still collected for some missions. Still images were collected from the underside of the landing deck for the Phoenix and InSight [1,19,39] which were used for post landing crater reconstructions. Images and videos were also collected during the Mars Science Laboratory [40,41] and Mars 2020 [41] providing information related to the onset of dust motion on the Martian surface during descent. A reconstruction of surface cratering from the Mars Science Laboratory Sky Crane procedure can be found in Vizcaino and Mehta [40].

Different data collection techniques were used to capture crater formation over the course of test campaigns. Experimental techniques like X-ray imaging [24] and direct measurements were common for early tests [17,27,28]. Recent PSI experiments utilize a clear splitter plate, which is an intrusive observation technique that allows for direct view of the crater; however, this geometry also likely affects plume structure and development. This has been used for subsonic studies [14,15,42], pulsed jet impingement [19], and supersonic impingement under low background pressure [43–45]. Alternatively, non-intrusive test configurations are in use or are in development to create reconstructions of crater formation through stereographic imaging [21,22,46]. These updated methods are also being used for individual particle tracking to characterize ejecta phenomena [47].

Despite a seemingly large number of experiments, there is a significant lack of time varying crater formation data spanning a wide range of operating conditions. The majority of available data is for stationary jets collected under subsonic, incompressible conditions, where erosion physics are different compared to flight landing environments. While descending jets are more representative of planetary landing, experiments of this kind were limited, and date back to the Apollo and Viking eras. For relevant older experiments involving compressible jet impingement, information on operating conditions is limited or non-existent, making it challenging to utilize available data. Fortunately, there has been a recent drive to expand available data sets to better characterize PSI for future missions, albeit for stationary jet impingement [21,22,43–46]. Additional flight observations of PSI are being attempted during landing based missions [48]. One example is the Stereo Cameras for Lunar Plume-Surface Studies (SCALPSS) system which was used to collect video of erosion and crater during the recent Firefly Blue Ghost landing on the Moon [49]. Because data for descending jets is limited, the work presented in the following sections focuses on a modeling framework for stationary jets that can be extended and validated for descending systems in the future, when more relevant experimental data are available.

1.3. High fidelity computational models and methods

For continuum environments, multiphase Computational Fluid Dynamics (CFD) can be used to directly simulate crater formation. Simulations typically require a combination of multi-scale approaches including direct numerical simulations to capture flow-structure interactions and Eulerian-Lagrangian or Eulerian-Eulerian methods for particle tracking and/or crater formation [10,50–52]. Eulerian-Lagrangian simulations capture individual particle motion through aerodynamic forcing as well as particle-particle interactions; however, they can also be computationally expensive [10,51]. Eulerian-Eulerian simulations

are an alternative approach where the gas and granular phases are both simulated as continuum fluids [50,52]. While these methods are less expensive, they can introduce errors into predictions for low particle volume fractions where the granular phase violates the continuum approximation. In addition, traditional Eulerian-Eulerian approaches are not built with granular mechanics in mind, and after a jet is throttled down in a simulation, the Eulerian crater can collapse and return to a non-physical flat surface.

Under vacuum conditions, the near-field flow around the nozzle exit is typically in a continuum regime. However, as the plume expands, inter-molecular collisions decrease in the exhaust, and the flow becomes increasingly rarefied. For these conditions the continuum assumption is no longer valid, and computations require the use of rarefied flow solvers such as the Direct Simulation Monte Carlo (DSMC) technique or a direct Boltzmann solver. Such techniques have been implemented to capture the continuum to rarefied transition for PSI events for lunar landing [53–55] usually implemented with one-way coupling between continuum and rarefied solvers. Other methods have been in development, adding two-way coupling capabilities to properly capture plume expansion [6].

Due to the complex nature of particle-fluid interactions and compressible turbulence, many of these methods, while promising, are still in their infancy. CFD methods require closure models to correct for scales below the grid resolution, including pseudo-turbulence effects [51]. Because modeling closure for these cases are nonexistent or not valid in simulation regimes, it is common for methods to pull from existing single phase closures for multiphase applications [50]. In addition, many of these models and methods have not been validated against experimental data. Improvements must be made to these models and methods before extending them to full scale engineering applications, like planetary landing events [2].

1.4. Reduced-order models and methods

The earliest model to predict erosion during a spacecraft landing was derived during the Apollo era [12,13]. Commonly referred to as the “Roberts model”, the original formulation and other variations [17,56] involve the estimation of shear stress on a surface followed by a calculation to determine the rate of granular entrainment during jet impingement. This leads to the formation of an annular crater which can be explained by the variation of stress on the surface relative to the stagnation point, where shear is zero. For cases where erosion occurs, granular material is prescribed with a velocity in order to calculate a mass flux from the surface. The granular velocity is defined by a series of empirical correlations and correction factors, including the hypersonic parameter, $k_{\text{hyper}} = \gamma(\gamma - 1)\text{Ma}^2$. Note that this term must be treated with care — additional details including the derivation, treatment, and interpretation of this parameter are included in Appendix A.

Recent manuscripts were published on scaling erosion behavior for plume-surface interaction applications for lunar environments [57–59]. Similar to saltation theory, these works describe erosion as an energy driven process, where the energy of the plume must overcome the granular potential to induce erosion. This work originally proposed as a functional fit with a log scale in Metzger et al. [14,18]. A similar approach, proposed in Morris et al. [60], assumes that mass flux of granular material is proportional to the densimetric Froude number. These methods follow the same general description where,

$$\phi_e \propto \frac{\rho_g u_g^2}{2g\rho_p d_p} = \text{Fr}^2. \quad (1)$$

Here, ϕ_e is the mass flux of eroded granular material, ρ_g is the gas density, u_g is the gas velocity, g is the acceleration due to gravity, ρ_p is the particle density, d_p is the particle diameter, and Fr is the Froude number. The dynamic pressure ($\rho_g u_g^2/2$) is evaluated above the impinging surface, and is used to evaluate erosion in terms of local

mass flux for rarefied conditions. For scaling purposes, it is common to fit against past observations [57,58,60] to match Apollo estimations. Other scaling approaches are also available such as arctangent functional fits from LaMarche and Curtis [15], and alternative descriptions of non-dimensional analysis in Mehta [1]. The choice of the arctangent functional fit from LaMarche and Curtis [15] appears to match well against experimental data due to the asymptotic nature of crater formation for fixed height impingement, as opposed to the log-function from Metzger et al. [14,18] and Metzger [57,58] which is unbounded and grows unphysically to infinity for large times compared to the experiments collected under finite atmospheric conditions.

Image processing techniques have also been used to estimate erosion after landing. Originally proposed by Lane and Metzger [26] and adopted by other groups [61,62], the optical extinction approach comes from correlations of radar degradation in the presence of rainfall [63, 64]. While some useful data can be extracted with this technique, there are limitations to this method. For example, in the presence of larger dust concentrations images become saturated which can obscure the total amount of material eroded during descent. This model also relies on the optical properties of the granular material which requires additional tuning depending on the application and landing environment.

While the listed methods are described and used in literature, there is still a lack of comparisons against experimental data for a wider range of operating conditions. In the following sections, an alternative framework is proposed for reduced-order estimations of crater formation during plume impingement.

2. Non-dimensional analysis

When applied to various engineering problems, non-dimensional analysis can be a powerful approach to characterize behavior based on parameter space variation. Here one approach to non-dimensionalization is introduced and applied to plume-surface interactions. See Section 3 for a discussion on a model that uses the non-dimensional terms derived in this section.

2.1. Buckingham-Pi

The Buckingham-Pi approach has a storied history for modeling complex problems. This procedure was famously used by G.I. Taylor to estimate the energy output of the atomic bomb [65]. By making similarity arguments for the three dimensional expansion of a blast wave, one can elegantly construct an expression of radial variation of the wave as a function of time, energy, and fluid properties. Note that the approach is strictly for characterizing the non-dimensional terms associated with an engineering problem. With knowledge of the physics and important parameters for said problem, it is possible to determine non-dimensional parameters and construct models as seen in Szirtes [66], Gibbins [67] and Chemloul [68].

The process begins with outlining the variables of interest for an engineering problem. This is followed by determining the number of independent dimensions and selecting variables to represent said dimensions. With a proper selection, the number of non-dimensional terms for the system is equal to the number of variables minus the number of independent dimensions. The remaining terms are known as the dependent variables. Each non-dimensional term is discovered by solving a linear system of equations that consists of information of the dimensions for each independent variable for all respective dependent variables. A thorough discussion of the process and required math are included in Szirtes [66].

2.2. Non-dimensional terms for plume-surface interaction

For this analysis, the system in Fig. 1 is used. The flow parameters include the exit flow density (ρ_{exit}), velocity (V_{exit}), pressure (P_{exit}), and viscosity (μ). Variables describing the environment and jet include time (t), atmospheric pressure (P_{atm}), atmospheric density (ρ_{atm}), gravity (g), height of the jet above the granular bed (h), nozzle exit diameter (d_{jet}). Finally, the granular properties and resulting crater formation are described by mean particle diameter (\bar{d}_p), particle density (ρ_p), porosity (n), width of crater (w_c), and depth of the crater (d_c). For the purposes of modeling, it is assumed that the crater depth and width are independent and can be characterized by the flow, granular, and environmental conditions as inputs to the system.

Other terms like cohesion, angle of repose, and particle shape were purposely neglected in this analysis. Regarding cohesion, past observations, through saltation theory [69,70], show that highly cohesive granular material tends to lead to different thresholds of erosion. Given the complex nature of particle shape and adhesion [71–75], directly characterizing these effects with limited observations is challenging. In this manuscript, cohesion is not directly accounted for due to uncertainties in modeling procedures and operating conditions. Additional details can be found in Appendix C. This assumption is comparable to the Holsapple scaling equations for kinetic impactor crater formation where the strength of the material, effectively a cohesion term, is set to zero for sand and similar granular materials [76]. Regarding angle of repose, the slope of the interior walls of a crater regularly exceed this angle as the flow actively keeps walls from collapsing during impingement [15,18,20]. This observation, combined with the fact that angle of repose is linked particle properties like diameter, means it may be redundant for scaling arguments. As additional data becomes available, parameters can be added to expand fitting operations.

Because there are a large number of variables relevant for the problem, it is advantageous to combine them and possibly reduce the number of non-dimensional terms that arise in the analysis. This can be achieved by combining relevant variables for analysis. For example, exit velocity and density can be combined into a dynamic pressure (P_{dyn}) while particle density and porosity are combined to form bulk density (ρ_{bulk}). Note that leading factors, such as “1/2” for dynamic pressure, are omitted in this analysis. With these changes, there are 13 modeling parameters which span three reference dimensions, mass, length, and time. As a result, there will be 10 non-dimensional Pi -terms for the parameter space. For the non-dimensionalization, dynamic pressure, bulk density, and the jet diameter are selected as the independent variables.

The non-dimensional system with the described independent variable results in the following Pi -terms,

$$\begin{aligned} \Pi_{1,o} &= d_c/d_{\text{jet}}, & \Pi_{2,o} &= w_c/d_{\text{jet}}, & \Pi_{3,o} &= P_{\text{dyn}}^{1/2} t / d_{\text{jet}} \rho_{\text{bulk}}^{1/2} \\ \Pi_{4,o} &= \mu / \rho_{\text{bulk}}^{1/2} P_{\text{dyn}}^{1/2} d_{\text{jet}}, & \Pi_{5,o} &= \bar{d}_p / d_{\text{jet}}, & \Pi_{6,o} &= P_{\text{atm}} / P_{\text{dyn}}, \\ \Pi_{7,o} &= P_{\text{exit}} / P_{\text{dyn}}, & \Pi_{8,o} &= g d_{\text{jet}} \rho_{\text{bulk}} / P_{\text{dyn}}, & \Pi_{9,o} &= h / d_{\text{jet}}, \\ & & \Pi_{10,o} &= \rho_{\text{atm}} / \rho_{\text{bulk}}. \end{aligned}$$

The subscript ‘o’ indicates the terms that are a direct result of the Buckingham-Pi procedure. While terms are unique from the process, they can be combined to reduce the number of dimensions used for fitting later in the manuscript. This is possible because the product of non-dimensional terms is also a non-dimensional term. Above, $\Pi_{1,o}$, $\Pi_{2,o}$, $\Pi_{5,o}$, and $\Pi_{9,o}$ are independently varying length scales. Rearranging $\Pi_{4,o}$, leads to a Reynolds number based on mixture density, $\text{Re} = (\rho_{\text{exit}} \rho_{\text{bulk}})^{1/2} V_{\text{exit}} d_{\text{jet}} / \mu$. This term can be multiplied by the square root of the density ratio to strictly be a function of the gas phase. Combining $\Pi_{6,o}$ and $\Pi_{7,o}$ results in a pressure ratio, $\text{PR} = P_{\text{exit}} / P_{\text{atm}}$. By expanding $\Pi_{8,o}$ results in the densimetric Froude number, $\text{Fr}_\rho = V_{\text{exit}} / (g d_{\text{jet}} \rho_{\text{bulk}} / \rho_{\text{jet}})^{1/2}$. Finally, one can rearrange $\Pi_{3,o}$, giving $\rho_{\text{exit}}^{1/2} V_{\text{exit}} t / (\rho_{\text{bulk}}^{1/2} d_{\text{jet}})$. This final term is not discussed in literature and

is interpreted as a ratio of energies between the impinging flow and granular media. This can be realized by the following expression,

$$\frac{\Pi_{\rho_{\text{bulk}}}}{\Pi_t^2} = \frac{1}{\Pi_{3,o}^2} = \frac{\rho_{\text{bulk}} (d_{\text{jet}}/t)^2}{\rho_{\text{exit}} V_{\text{exit}}^2} = \frac{\text{Energy for granular excavation}}{\text{Kinetic energy of flow}}. \quad (2)$$

Here, the energy imparted on a granular media is balanced by the energy to “excavate” granular material over some characteristic length scale, in this case d_{jet} . The expression can be modified to be in terms of the particle diameter, by taking the product between $\Pi_{5,o}$ and Π_t , which more intuitively describes the rate of removing “layers” of granular material from an affected area. While the behavior of this term is only demonstrated for gas-particle flows later in the manuscript, it is anticipated that the term can be extend to other related applications, such as water-jet impingement on granular media [7,77], due to the dependence on density.

After combining and rearranging relevant Pi -terms, the method results in a system of non-dimensional terms that will be used for the remainder of the paper,

$$\begin{aligned} \Pi_{d_c} &= d_c/d_{\text{jet}}, & \Pi_{w_c} &= w_c/d_{\text{jet}}, & \Pi_{1,t} &= \left(\frac{V_{\text{exit}}}{d_{\text{jet}}/t} \right), \\ \Pi_{2,d_p} &= \bar{d}_p/d_{\text{jet}}, & \Pi_{3,\rho_{\text{bulk}}} &= \rho_{\text{bulk}}/\rho_{\text{exit}}, & \Pi_{4,h} &= h/d_{\text{jet}}, \\ \Pi_{5,\text{Re}} &= \frac{\rho_{\text{exit}} V_{\text{exit}} d_{\text{jet}}}{\mu}, & \Pi_{6,\text{PR}} &= P_{\text{exit}}/P_{\text{atm}}, & \Pi_{7,\text{Fr}} &= \frac{V_{\text{exit}}}{\sqrt{g d_{\text{jet}}}}, \\ & & \text{and } \Pi_{8,\rho_{\text{atm}}} &= \rho_{\text{atm}}/\rho_{\text{exit}}. \end{aligned}$$

For this analysis, it is noted that other independent variables can be selected for non-dimensionalization. This is a choice and improper selection can lead to mathematically ill-posed, undefined, and/or non-trivial Pi -terms. Here the choice of independent variables was made through a rigorous process. For example, an alternative choice would involve selecting time, t , instead of dynamic pressure, P_{dyn} , to treat dimensional time in the remaining dependent variables. Unfortunately this leads to multiple time dependent Pi -terms, as opposed to a single isolated term, making it more difficult to construct a model in the following sections.

3. Modeling framework

For a system of n parameters, it is assumed that a Pi -term can be represented as a function of the remaining terms,

$$\Pi_a = f(\Pi_1, \Pi_{i+1}, \dots, \Pi_n). \quad (3)$$

In prior works, both natural logarithms [14] and arctangent functions [15] have been used as the modeling function. Arctangent has the benefit of being asymptotic as the domain variable approaches infinity while also being equal to zero at the origin, unlike a natural logarithmic function. The asymptotic nature of crater formation is characteristic of finite atmospheric environments [15]; however, this is not always true for near-vacuum conditions where linear or exponential crater growth has been observed [78]. The modeling function is ultimately a choice as long as each non-dimensional term can be written as a function of all remaining non-dimensional terms, as described in Eq. (3). Here a product of power functions is used to capture different crater formation rates regardless of operating condition,

$$\Pi_a = C_a \prod_{i=1}^n \Pi_i^{\alpha_i}. \quad (4)$$

In Eq. (4), C_a is a model constant and α_i is the power variation for the i th Pi -term. The power function is also commonly used for other scaling problems in Szirtes [66].

For the purposes of modeling length scale variation, such as the depth of the crater, the system can be written as,

$$\frac{d_c}{d_{\text{jet}}} = C_a \prod_{i=1}^n \Pi_i^{\alpha_i} = C_a \left(\prod_{i=2}^n \Pi_i^{\alpha_i} \right) \Pi_{1,t}^{\alpha_{1,t}}. \quad (5)$$

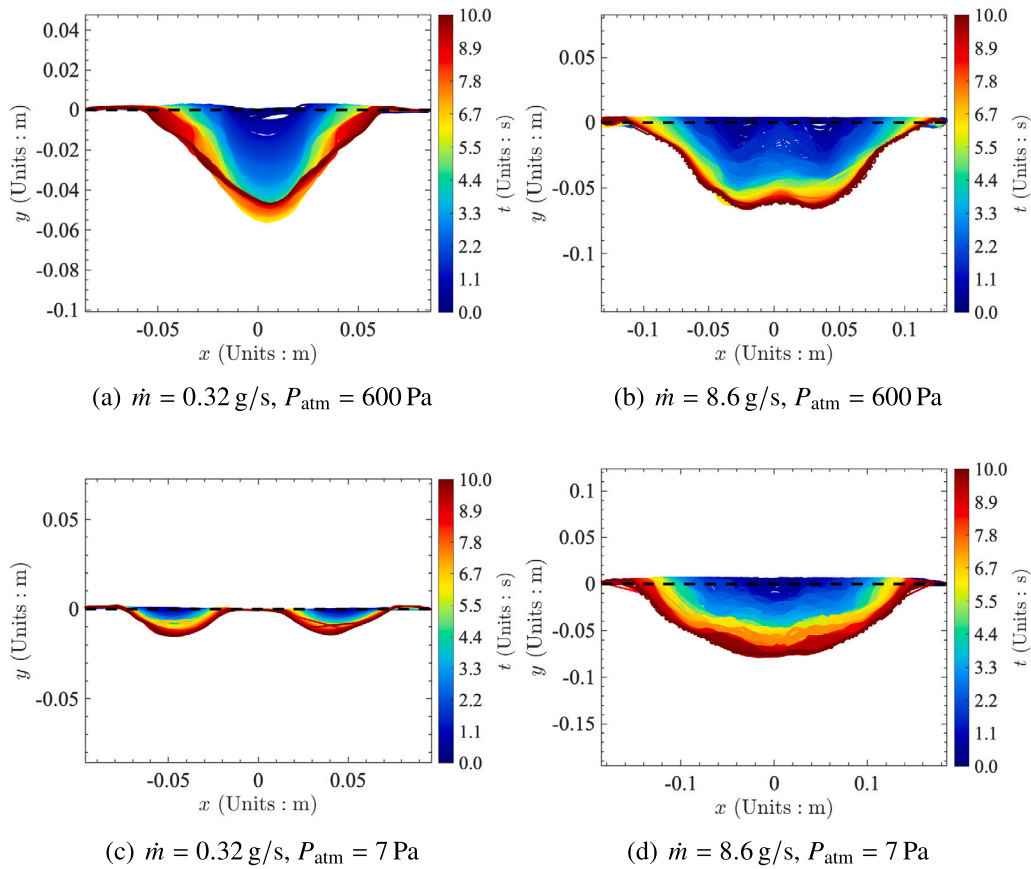


Fig. 3. Crater evolution plots for (a) R13-MDS (over-expanded), (b) R10-MDS (under-expanded), (c) R1-MDS (under-expanded), and (d) R9-MDS (under-expanded). Data collected from Korzun et al. [43]. A summary of conditions can be found in Appendix B.

The non-dimensional excavation rate term is factored out to show the variation of depth is a function of time. The same equation structure holds when modeling crater width. It is acknowledged that depth and width are coupled through the volume of a crater; however, as pointed out in Section 1.1, crater shapes and volumes vary depending on operation conditions. Separating the length scales simplifies the analysis, allowing the user to adapt the model to the appropriate crater shape for volume estimations.

Another approach is proposed in Gorman et al. [79] which scales erosion assuming that it acts as an analogy to the kinetic impactor [80]. The intent for the formulation proposed in Holsapple [80] is an instantaneous interaction between a mass and granular media for crater formation. As shown in later sections, timescales of interaction are large relative to instantaneous meteorite impacts. Gorman et al. [79] also utilizes multiple rates of crater formation in time. If a user would like to model multiple rates, fits can be performed for ranges of time and smoothing functions can be applied between functions similar to Eq. (5). In this manuscript, the simplified single rate formation is used and multi-rate functional behavior is addressed in Section 4.

3.1. Experimental data and fitting operation

Ideally, modeling parameters from Section 2 would be derived from experimental data exhibiting wide parameter space variation. Unfortunately, data for plume-surface interactions is rather sparse, especially for high speed, reacting flows [43–45].

Experimental data is from [15,20,43,81]. For the included data, there are variations of flow conditions for the velocity, height, jet diameter, particle density and size variation, and pressure ratio. This includes flows ranging between incompressible and compressible, $Ma_e \leq$

5.3, impingement on granular beds. Background pressure varies between standard atmospheric pressure and $P_{atm} = 2.67$ Pa. Granular media includes material with $\bar{d}_p = O(10^1 - 10^3) \mu m$ with $\rho_{bulk} = O(10^2 - 10^3) kg/m^3$. Additional details on operating conditions separated by experiment as well as reference case numbers, plot symbols, and colors used to identify experimental data in Section 4 can be found in Appendix B and ranges for non-dimensional numbers for fitting can be found in Section 3.2. Note that other experiments exist in literature; however, one must be careful when considering their inclusion. For example, the non-symmetric test stand in Guleria and Patil [42] would introduce error into fitting operations and other reports lack details on operating conditions to compare to data [25].

Fitting is performed with the built-in MATLAB least squares curve fitting operation (lsqcurvefit) along with the 'trust-region-reflective' algorithm [82]. The operation is performed with setting the max number of iterative solves and function evaluations to an arbitrary larger number. The function and optimality tolerance are set to $100 \times \epsilon$, where ϵ is machine precision, while the finite difference derivative step of $\Delta x_{deriv} = 1 \times 10^{-10}$ is used. To ensure the rate of crater formation decreases in time for operating conditions involving finite atmospheric conditions, as observed in past experiments [14,15], the non-dimensional time exponent, $\alpha_{1,t}$, was bound between zero and one for the majority of cases. Other power coefficients were allowed to vary between ± 5 or ± 10 if a solution is not found, while the leading coefficient was allowed to vary between 0 and 100.

Other methods to fit sparse datasets are available in literature; however, the main focus of this work is the model formulation. To address errors in the described method, an uncertainty analysis is provided in Appendix D including discussions on fitting parameters and the root mean square error of the model relative to experimental data.

Table 1

Range of non-dimensional numbers for fitting, shown as [minimum, maximum], for $\Pi_{1,f}$, Π_{2,d_p} , $\Pi_{3,\rho_{bulk}}$, $\Pi_{4,h}$, $\Pi_{5,Re}$, $\Pi_{6,PR}$, $\Pi_{7,Fr}$, and $\Pi_{8,\rho_{atm}}$. Data is separated by regime of fitting including over-expanded (OE), ideal-expanded (IE), under-expanded (UE), and under-expanded near-vacuum (UE-NV) conditions.

| Regime | $\Pi_{1,f}$ | Π_{2,d_p} | $\Pi_{3,\rho_{bulk}}$ | $\Pi_{4,h}$ |
|--------|--------------------|------------------|-----------------------|----------------------|
| OE | [671, 8.36e5] | [0.0108, 0.0201] | [5.91e5, 7.24e5] | [3, 10] |
| IE | [30, 3.84e5] | [0.006, 0.159] | [555.83, 4095] | [6.49, 70] |
| UE | [671, 6.68e5] | [0.0108, 0.0108] | [2.68e4, 2.68e4] | [3, 10] |
| UE-NV | [671, 9.59e5] | [0.0108, 0.147] | [1170, 7.24e5] | [3, 37.1] |
| Regime | $\Pi_{5,Re}$ | $\Pi_{6,PR}$ | $\Pi_{7,Fr}$ | $\Pi_{8,\rho_{atm}}$ |
| OE | [5856, 5856] | [0.083, 0.186] | [2536, 2536] | [1.39–3.14] |
| IE | [1.07e4, 1.41e5] | [1, 1.09] | [76, 1474] | [0.77, 1] |
| UE | [1.584e5, 1.584e5] | [2.23, 5.00] | [2536, 2536] | [0.0516, 0.116] |
| UE-NV | [5856, 1.58e5] | [1.86, 3130] | [1456, 2536] | [2.76e–4, 0.14] |

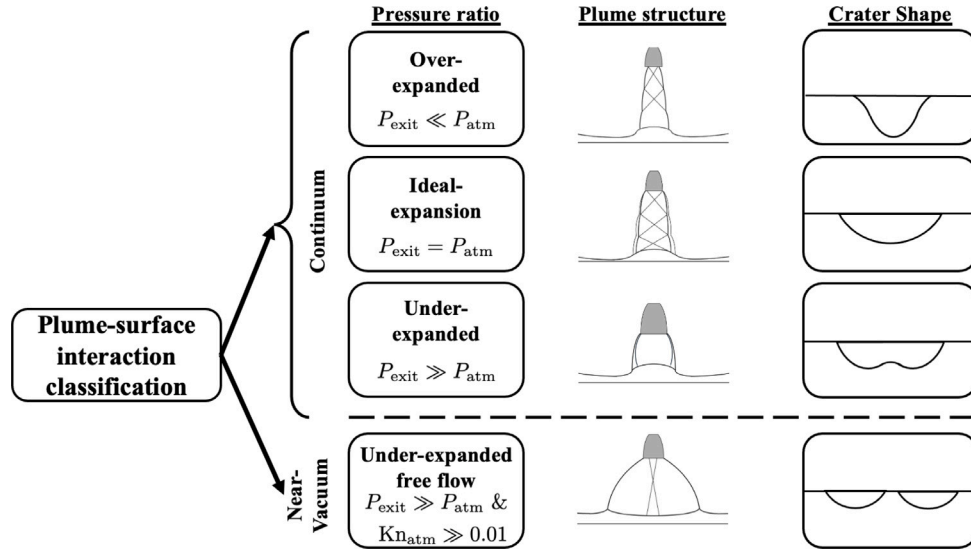


Fig. 4. Plume-surface interactions for different jet expansion ratios and corresponding crater shapes.

3.2. Flow regimes and crater formation

In literature it is common to perform parameter estimation based on the available data from a single experimental setup; however, this does not guarantee that relationships will capture a wide range of behaviors. For example, the plots in Fig. 3 show crater evolutions for some of the data collected from Korzun et al. [43]. Contrary to traditional definitions of crater formation described in Section 1.1, it is believed that crater shape and evolution is tied to the jet expansion ratio. This is explained by the differences in flow and shock structures that persist as a function of operating conditions. The interested reader can refer to Rodrigues et al. [83,84] for visualizations of experiments using planar laser-induced fluorescence (PLIF) or Vick et al. [85] for the original study attempting to classify different compressible structures as a function of jet expansion ratio for impingement.

Craters are therefore scaled in the following four categories which include: (1) over-expanded jets ($P_{\text{exit}} \ll P_{\text{atm}}$), (2) ideal-expansion ($P_{\text{exit}} = P_{\text{atm}}$), (3) under-expanded jets ($P_{\text{exit}} \gg P_{\text{atm}}$), and near-vacuum conditions ($P_{\text{exit}} \gg P_{\text{atm}}$ & $\text{Kn}_{\text{atm}} \gg 0.01$). A breakdown of crater shapes and expansion ratios are provided in Fig. 4. Here Kn_{atm} is taken to be the Knudsen number based on the nozzle diameter and ambient conditions at the landing site. Even though this parameter is independent of the thruster operating conditions, this can be used to estimate the flow behavior far away from nozzle exit conditions. Because the data is split into four regimes, the ranges of operating conditions have specific ranges for each condition. These ranges can be found in Table 1.

As jets expand into near-vacuum conditions, the flow becomes rarefied and erosion behaves differently compared to erosion under

continuum conditions. This motivates separating the under-expanded category into continuum and near-vacuum conditions. This can be observed by comparing the experimental data for under-expanded jet conditions under finite atmosphere and low vacuum in Figs. 10(a) and 14(a) respectively. The erosion rates are asymptotic for finite pressure and exhibit exponential growth for low vacuum environments. While this behavior is observed, it is noted that the asymptotic behavior is recovered for near jet impingement where the jet behaves as a continuum [22,81].

4. Results

In this section the tools and methods from Section 3 are used in combination with experimental data described in Section 1.2 to demonstrate the crater modeling framework for PSI analysis. To reiterate, fitting is performed through power law variation of the Pi -terms. First gravitational scaling is addressed since nearly all available experimental data is collected under Earth gravity. Then the modeling procedure is shown for the time variation of depth and width for four crater formation regimes. These include over-expanded, ideal-expanded, under-expanded, and near-vacuum jet impingement.

4.1. Gravitational scaling

As discussed in Section 1.4, it is common to scale erosion rate relative to gravitation acceleration and nozzle exit conditions [20,57, 58,60]; however, there is limited data to do so. This is because gravity variation requires using a drop tower [86] or parabolic flights [20] during impingement studies. To avoid these expensive techniques, other

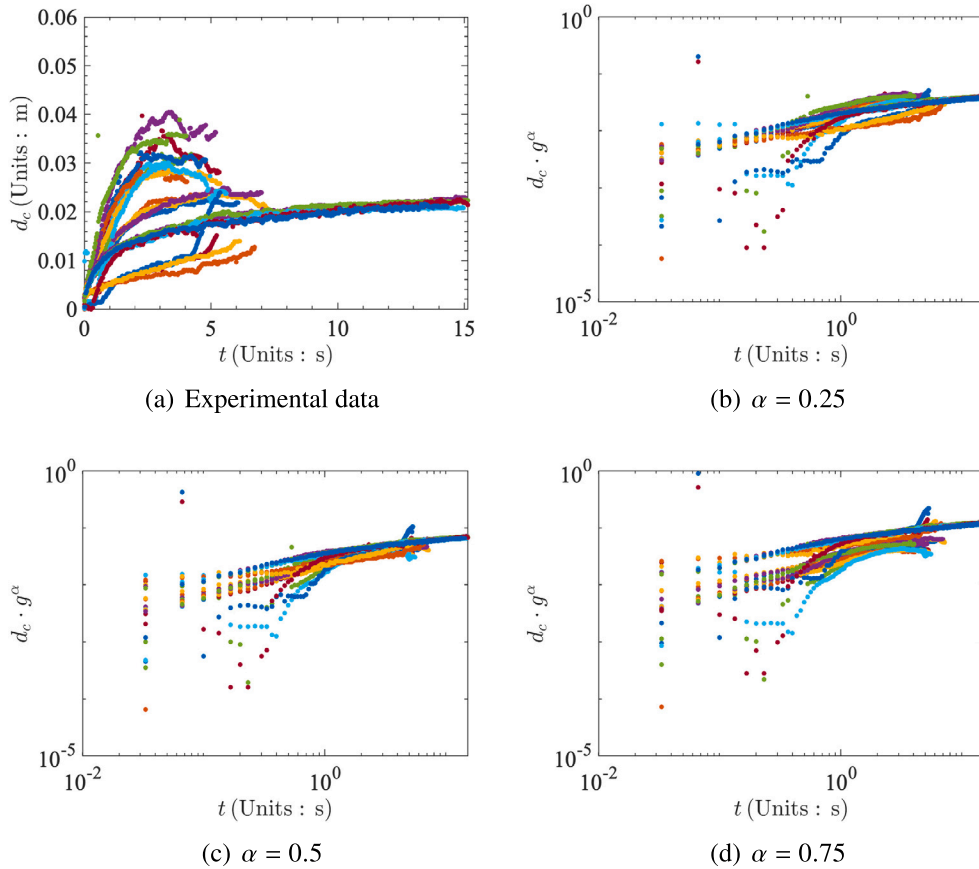


Fig. 5. (a) Experimental data for crater depth from Metzger et al. [20] and collapse of experimental data using (b) $\alpha = 0.25$, (c) $\alpha = 0.5$, and (d) $\alpha = 0.75$.

works have proposed using lower density granular material, like walnut shells, to mimic gravitational variation [1,19,87]. This choice should be avoided in future experimental studies. While lower density granular material modifies the densimetric Froude number, it also modifies the particle Stokes number, $Stk = \tau_p/\tau_f$, by lowering the particle reaction timescale, τ_p , relative to the fluid timescale, τ_f . As a result, particles react to the surrounding flow much quicker than standard regolith would for scaling purposes. Here, analysis strictly considers parabolic flight data. Unfortunately, the majority of data involving gravity variation is for subsonic incompressible flows at standard Earth atmospheric conditions. This will not cover all jet expansion ratios described in Section 3.2. Here a power scaling of Froude number is calculated for crater depth and width and assumed to be constant under all flow regimes. To be clear this is not ideal and is a placeholder until data is collected for a wider set of conditions, such as near-vacuum studies under modified gravitational conditions.

Data from a series of experiments described in Metzger et al. [20] are used for gravitational scaling. These experiments were collected on parabolic flights to evaluate the effect of varying acceleration on erosion rate for the same operating conditions. This included standard Earth, 9.81 m/s², lunar 1.62 m/s², Martian, 3.73 m/s², and hyper-gravity, 19.62 m/s². Data is provided for two granular materials: sand and JSC-1a. Unfortunately, the operating conditions for the jet were not provided, nor were collected, for each dataset. If all operating conditions remained consistent between experiments, the Froude number can be scaled by directly via a power-law variation of gravity whereby,

$$\Pi_{Fr}^{\alpha_{Fr}} = \left(\frac{V_{exit}}{(gd_{jet})^{1/2}} \right)^{\alpha_{Fr}} = Cg^\alpha, \text{ with } C = \left(\frac{V_{exit}}{(d_{jet})^{1/2}} \right)^{\alpha_{Fr}} \text{ and } \alpha_{Fr} = -2\alpha. \quad (6)$$

By evaluating data collapse when multiplying by power variations of gravity, the dependence on Froude number can be calculated with limited information on the operating conditions. The best fit is determined with a linear least squares fit of the scaled data in log-space for the 22 experiments involving sand. Using the root mean square error (RSME) of the data relative to the fit, the lowest error for a range of α 's indicates the best gravitational scaling.

With this procedure, the raw data and collapse of data for various α is shown in Figs. 5 and 6 for depth and width respectively while the RMSE is shown in Fig. 7. Here the best collapse of crater depth data is observed for $\alpha = 0.455$ or a Froude number scaling of $\alpha_{Fr} = -0.91$. The same process is repeated for crater width data with the most noticeable collapse occurring for $\alpha = 0.14$ or a Froude number scaling of $\alpha_{Fr} = -0.28$. See Fig. 6 for a comparison of collapse of crater width under different values of α .

Due to the dependence of erosion rate on operating conditions, discussed in Section 4.2, it is recommended that gravitational scaling should be evaluated for a wider range of operating conditions. To check if the scaling coefficient is consistent between studies, the values are compared to the Froude scaling for crater depth discussed in Sonar and Katsuragi [86]. In the referenced work, data is scaled as a function of the erosion number, E_c which is a function of gravity and originally introduced in Rajaratnam and Beltaos [88],

$$E_c = Fr \sqrt{\rho_{atm} / (\rho_g - \rho_{atm})} d_{jet} / h, \quad (7)$$

where Froude number is calculated as $Fr = V_{exit} / \sqrt{gd_p}$. This shows that gravity varies with $\alpha = 0.5$, which is close to the value found by scaling the data in Metzger et al. [20]. This provides confidence in the gravity scaling used for the remainder of this work.

Regardless of the observed collapse of data, Sonar and Katsuragi [86] concluded that the described gravitational scaling was not appropriate due to scatter observed in their data. These conclusions are

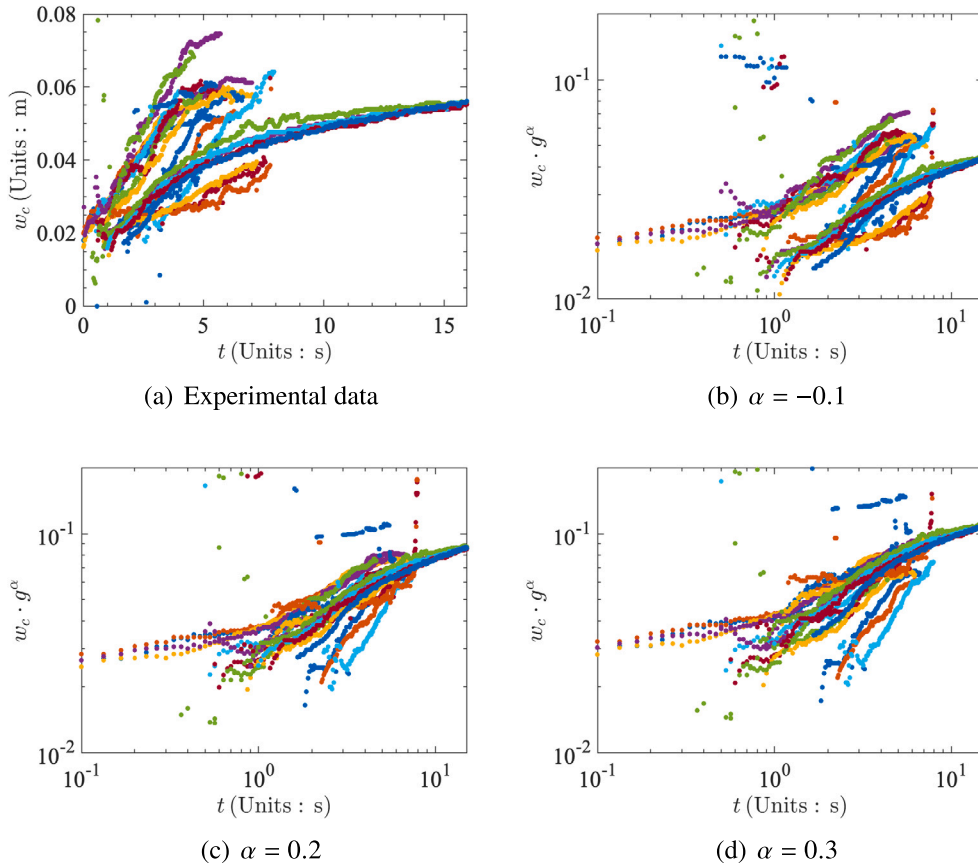


Fig. 6. (a) Experimental data for crater width from Metzger et al. [20] and collapse of experimental data using (b) $\alpha = -0.1$, (c) $\alpha = 0.2$, and (d) $\alpha = 0.3$.

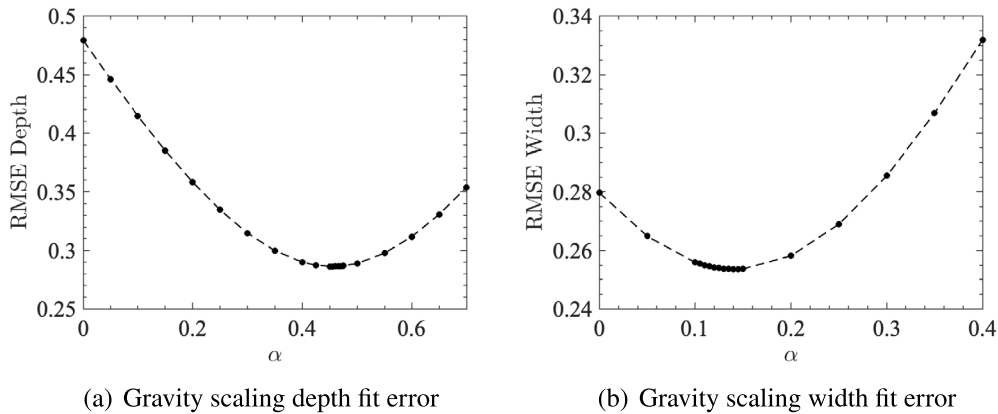


Fig. 7. Root mean square error (RMSE) for log space fit of (a) depth scaling and (b) width scaling for gravity.

somewhat misleading. As described above, Froude number in Sonar and Katsuragi [86] is calculated using the particle diameter as the reference length scale. Because change in crater depth can vary with particle diameter and granular properties, which are independent of operating conditions, scaling should be performed with separate terms. Using a different length scale for Froude number such as a constant jet diameter and including a separate scaling for particle diameter, or vice versa, could alleviate their observed data scatter.

4.2. Results for continuum conditions

The modeling procedure from Section 3 was applied to over-expanded, ideal expansion, and under-expanded jet impingement separately. Operating conditions for the experiments used in the analysis can be found in Appendix B. Because this method is used to capture time varying crater depth and width for stationary jet impingement, some datasets described in Section 1.2 were omitted for this analysis.

Table 2Crater depth modeling coefficients for each class of expansion ratio. Froude scaling, $\alpha_{7,Fr}$, is held at -0.91 for all regimes.

| Jet expansion ratio | C_0 | $\alpha_{1,t}$ | α_{2,d_p} | $\alpha_{3,\rho_{bulk}}$ | $\alpha_{4,h}$ | $\alpha_{5,Re}$ | $\alpha_{6,PR}$ | $\alpha_{8,\rho_{atm}}$ |
|---------------------|-------|----------------|------------------|--------------------------|----------------|-----------------|-----------------|-------------------------|
| Over | 1.00 | 0.36 | 0.83 | 4.09 | −0.41 | −4.91 | 3.30 | 3.44 |
| Ideal | 0.10 | 0.19 | −0.07 | −0.69 | −0.81 | 1.26 | – | −7.13 |
| Under | 2.76 | 0.66 | −6.73 | 7.54 | 0.63 | −8.76 | 2.28 | 2.70 |
| Near-vacuum | 2.77 | 1.02 | −0.36 | −0.37 | −1.21 | 0.47 | 3.22 | 3.71 |

As mentioned, the majority of historical datasets from the Apollo and Viking eras utilized descending nozzles, usually measuring the final crater depth and width as opposed to the variation in time. Raw data presented in Sonar and Katsuragi [86] also appears to look at static values; however, raw videos appear to be available online for the interested reader to process.

As previously highlighted, data is extremely limited for scaling analysis. This means that fitted power coefficients, apart from the time scaling ($\alpha_{1,t}$), are not always unique. A demonstration of uncertainty analysis is provided in Appendix D to address this point. For ideal-expansion cases, fitted coefficients are the median values. Single non-unique fits are shown for other regimes due to data limitations. Results for crater depth and width fitting coefficients can be found in Tables 2 and 3 while the root mean square error (RMSE), where $RMSE = \sqrt{(\sum_{i=1}^n (y_{i,data} - y_{i,model})^2)/n}$, is reported for the fitted values in Table 4. The power coefficients for pressure ratio are purposefully blank for the ideal expansion where the ratio is near unity, therefore power-law scaling is ineffective and therefore is neglected. The model was able to capture data variation with some noticeable deviations between the model and experiment, see Figs. 8–13 for plots of the data, model, and relative error for depth and width respectively.

The largest errors for all models are observed for early impingement times. For modeling purposes, multi-rate functions could be used to correct for early impingement behavior. For example, in Gorman et al. [79], there is a discussion that erosion rate transitions from between early and late stage behaviors. Other than the initial transients, there were no observed inflection points or sustained changes in erosion dynamics that would motivate the use of a multi-power law function. It is unclear if this is an effect for earlier transients during jet startup. Erosion rate transitions should be evaluated and isolated from transient behaviors in future studies like those from Stubbs et al. [22,81], which are collected over one second intervals. Other errors can be seen in the large oscillations in the erosion dynamics for different experiments from Korzun et al. [43]. This is from the regular collapse and recirculation of granular material during crater formation.

Another deviation between the experimental data and the model is observed for cases L1–L3 which correspond to glass sphere measurements with $\bar{d}_p = 46, 181, 250 \mu\text{m}$ from LaMarche and Curtis [15], see Figs. 12(a), 12(b), and 12(c). This indicates a non-trivial variation of crater width as a function of particle diameter, whereby the 181 μm results in a wider crater compared to the 250 and 46 μm particle sizes. This is not observed for scaling crater diameter, and requires additional experimental data for proper characterization. Another possible explanation comes from Bagnold [69], where the shear velocity to induce granular motion was observed to be larger for sufficiently small particles. Later it was determined that the “u-shape” relationship described in between particle diameter and shear velocity to induce motion from Bagnold [69] was due to cohesion of particulate [70] or rather smaller particles agglomerating and aerodynamically behaving like larger particles. To reiterate comments from Section 2.2, the effects of particle properties like shape and roughness should be explored once additional data becomes available.

4.3. Results for near-vacuum conditions

The process is repeated for crater width and depth for near-vacuum conditions. Results for crater depth and width fitting coefficients can be found in Tables 2 and 3. It is important to note that pressure rise is

expected for near-vacuum studies from Stubbs et al. [81] and Korzun et al. [43]. Here the initial ambient pressure is used for scaling purposes. Changes in ambient pressure will lead to variations in P_{exit}/P_{atm} in time; however, is considered to be out of scope of this work, which is a demonstration of the method. This is acknowledged and care should be taken for modeling and possible engineering applications of results.

Images for model predictions and comparisons to data can be found in Figs. 14 and 15. The model behaves well for crater width but has noticeable errors for crater depth. This is likely due to the nature of crater width which can be fairly constant for rarefied conditions. As for crater depth, there are deviations when comparing near- and far-field jet impingement [78,81]. This is likely due to the transition from rarefied to continuum flow and is expected to be predicted by a non-dimensional length scale. This will be similar to the continuum breakdown criterion from Bird [89], but will be based on operating and ambient conditions instead of local conditions. That being said, there is insufficient data to characterize this transition length scale and height dependent $\alpha_{1,t}$ for observed exponential and asymptotic crater depth evolution under a wide range of conditions. This will be important for engineering applications to rarefied landings, such as future missions to the Moon, where erosion behavior will not be constant as a function of impingement height.

4.4. Comments on general trends and physical mechanisms for crater formation

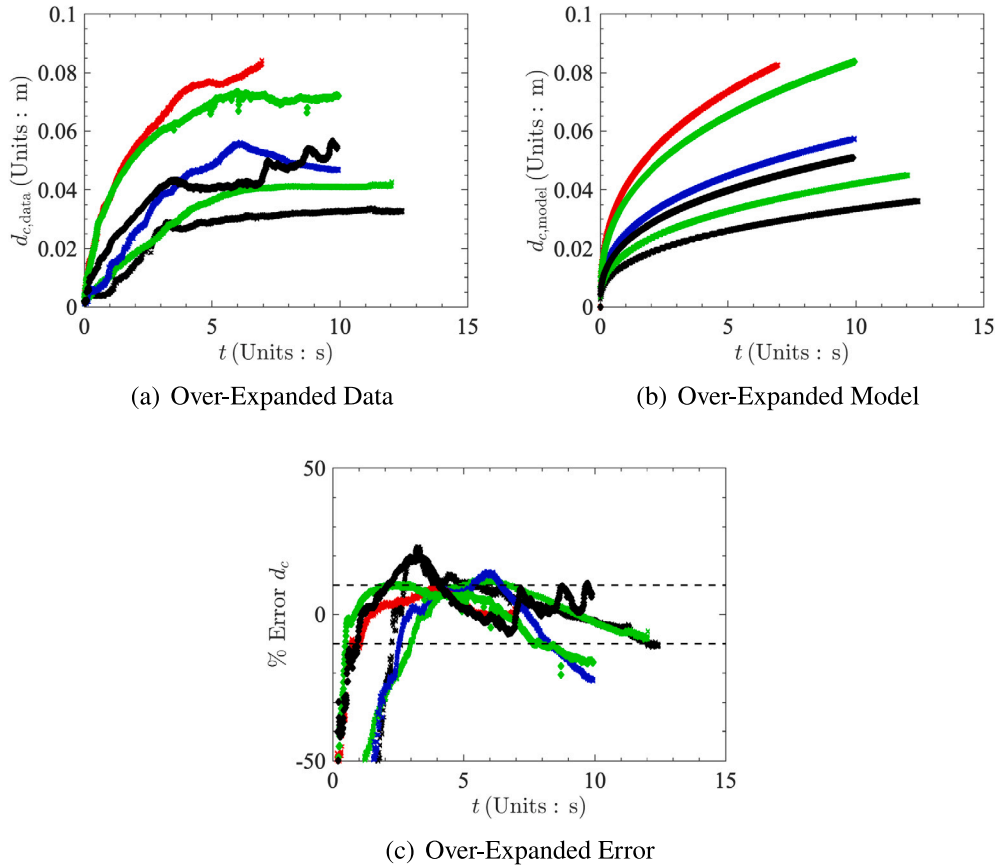
While constructed modeling errors can be relatively low, parameters for fitting with limited data, apart from $\alpha_{1,t}$, are not unique. This includes the over- and under-expanded regimes where limited data is available and non-dimensional parameters are largely invariant between experiments. The best and most consistent fit was observed for the ideal expansion cases, where operating conditions varied widely between experiments and data was collected using different test-setups.

The expressions in Tables 2 and 3 provide insight into the physics of crater formation for each of the regimes of interest. In general, $\alpha_{1,t}$ determines the rate of change for depth/width while remaining powers scale crater dimensions based on changes in jet and environment conditions. Fitting parameters with larger magnitudes indicate more sensitivity to variation in a particular non-dimensional number and the inverse is also true for smaller powers. While fitted trends do not specifically indicate the traditional mechanisms for crater formation described in Section 1.1 due to their phenomenological nature, it could provide insight into important physics for conditions of interest. For example, Reynolds number is defined as a ratio between the inertial and viscous forces in a fluid. If $\alpha_{5,Re}$ is positive this could indicate the dominance of inertial effects while negative values could indicate the dominance of viscous effects. Similarly, Froude number is defined as the ratio between inertial and gravitational forces. Positive values for $\alpha_{7,Fr}$ could indicate dominance of inertial forces while negative values could indicate dominant gravitational effects. Overall, values reported in Tables 2 and 3 are expected to change, along with interpretation of dominant regimes, as data is added to this analysis.

Additional data is also required properly characterize erosion behavior under a wide range of conditions as seen with the power variation in non-dimensional height. In Table 2, there is a positive correlation between crater depth and impingement height for under-expanded jets. This is counter intuitive since it implies that the crater depth does not increase with decreasing height. This is likely

Table 3Crater width modeling coefficients for each class of expansion ratio. Froude scaling, $\alpha_{7,Fr}$, is held at -0.28 for all regimes.

| Jet expansion ratio | C_a | $\alpha_{1,J}$ | α_{2,d_p} | $\alpha_{3,\rho_{bulk}}$ | $\alpha_{4,h}$ | $\alpha_{5,Re}$ | $\alpha_{6,PR}$ | $\alpha_{8,\rho_{atm}}$ |
|---------------------|-------|----------------|------------------|--------------------------|----------------|-----------------|-----------------|-------------------------|
| Over | 11.83 | 0.41 | -0.21 | -0.82 | -0.14 | 0.089 | -4.45 | -4.67 |
| Ideal | 6.40 | 0.24 | -0.002 | -0.41 | 0.009 | 0.22 | – | -4.26 |
| Under | 8.23 | 0.36 | 0.10 | -0.084 | -0.039 | -0.079 | -0.099 | -0.025 |
| Near-vacuum | 100 | 0.56 | -0.37 | -0.49 | -0.07 | -0.056 | 1.56 | 1.68 |

**Fig. 8.** Comparisons of crater depth (a) data, (b) model, and (c) error results for Over-Expanded jets. All experimental data is from [15,20,22,43,81]. A summary of conditions can be found in Appendix B. Experiments for over-expanded analysis include R141, R127, R13, R8, R7, and R15.

4.5. A discussion on existing scaling formulations

Additional manuscripts on scaling plume-surface interactions are available in literature [57,58,79,86]. While the models are not shown for comparison in Section 4, it is important to highlight the differences in the background formulations compared to the current model.

In Gorman et al. [79], power fitting is used to scale crater depth. It is found that early stage erosion scales as $O(t^1)$ while late stage erosion varies as $O(t^{1/3})$, both differing from the power law variations found in Table 2. Note that the functional form of early and late stage erosion is left open to interpretation to the reader, and the choice of variables for non-dimensionalization is not unique. That being said, improper choices can lead to terms without physical meaning, a mathematically ill-defined system, or a redundant parameter space for analysis.

Within Sonar and Katsuragi [86], scaling is performed for a set of drop tower experiments. The proposed scaling includes parameters like Mach number, Froude number, Reynolds number, and other non-dimensional length scales. The collapse of data is then shown for the final static measurements of crater formation as opposed to the evolution of cratering depth and width. Additional analysis on the behavior of the scaling would be interesting for flows exceeding sonic exit conditions.

Table 4

Root mean square error (RMSE) of fit relative to experimental data for depth and width using coefficients reported in Tables 2 and 3.

| Jet expansion ratio | Depth | Width |
|---------------------|--------|--------|
| Over | 0.0048 | 0.0063 |
| Ideal | 0.0041 | 0.0124 |
| Under | 0.0093 | 0.0162 |
| Near-vacuum | 0.0067 | 0.0457 |

because the majority of experiments from Korzun et al. [43] were collected for lower impingement heights, $h/d_{jet} \leq 10$. For low h/d_{jet} , a subsonic recirculation region is immediately above the surface and contained by the deflected expansion/compression waves [90,91]. These waves form an annular shock and thus an annular crater shape in regions of high shear when impinging on a granular surface. See Fig. 16 for an example of structures forming for under-expanded jet impingement and low and high h/d_{jet} .

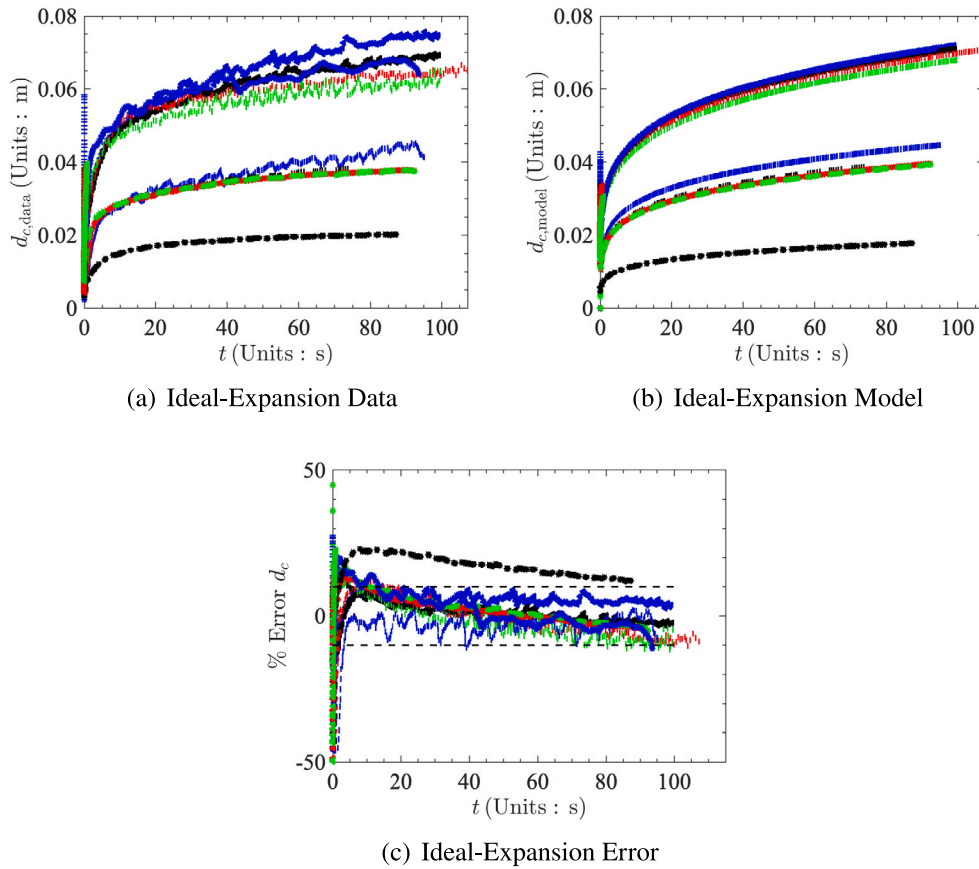


Fig. 9. Comparisons of crater depth (a) data, (b) model, and (c) error results for Ideal-Expansion jets. All experimental data is from [15,20,22,43,81]. A summary of conditions can be found in Appendix B. Experiments for expanded analysis include M1, M2, M3, M4, L1, L2, L3, L4, L5, L6, B1, B2, B3, and B4.

The model proposed in Metzger [57,58], briefly discussed in Section 1.4, scales crater formation based on a ratio between the dynamic pressure and gravitational potential of granular material. This Froude based scaling is modified to correct for cohesion effects between particles and better match experimental data. While promising, it can be challenging to properly characterize granular material properties like surface energy, Young's modulus, and Poisson's ratio used for cohesion models, see Appendix C for more details. In addition, this formulation is used in combination with a log-function to described the growth of crater dimensions which is not asymptotic and does not guarantee zero crater growth at the initial condition, unless the function is modified [15,86].

5. Conclusions

In this work, plume-surface interaction associated crater formation were modeled using non-dimensional analysis. A brief description of other approaches was provided such as those using numerical and semi-analytic methods. Following, a thorough derivation and description of relevant non-dimensional terms was given, along with a description of a new term that describes the balance of imparted energy by the flow and that which is required to move granular material. This method was then demonstrated using a fitting operation against existing experimental data. Comparisons with experiments were largely promising; however, need to be further evaluated as additional test data becomes available. Scaling of the available data showed the importance of time variation and jet expansion ratios on crater evolution. In summary,

this manuscript outlines an alternative modeling framework that can be extended and improved for engineering applications.

To reiterate, the method shown in this work is demonstrated for very limited data. It is desirable to apply the described model to physically relevant conditions applicable to engineering systems. For planetary landing, this would require experiments collected over larger timescales, using lower background pressures, and in the presence of descending jets. It is anticipated that the formation and evolution of compressible structures during descent would lead to different dynamics of crater formation. In addition, while common in literature, it is not recommended to make large extrapolations from the lower speed flow conditions to compressible, high speed operations.

Future studies should explore the behavior of non-linear regression methods on the resulting model solution as well as local minima sensitivity. This is expected to have minor impacts on fitting behavior; however, it is beneficial to characterize the best methods to fit sparse, time varying datasets for such problems.

Finally, as mentioned in the introduction, mechanisms are typically used to describe crater formation in literature, including diffusion-driven flow, diffused gas eruption, bearing capacity failure, viscous erosion, and diffuse gas explosive erosion [17–19]. These “effects” are completely phenomenological in nature. While helpful for described observed behavior for granular motion, they have limited utility for modeling purposes. A modification or re-characterization of effects during crater formation, grounded in timescales, thresholds, and geometric observations, are needed for improving modeling efforts.

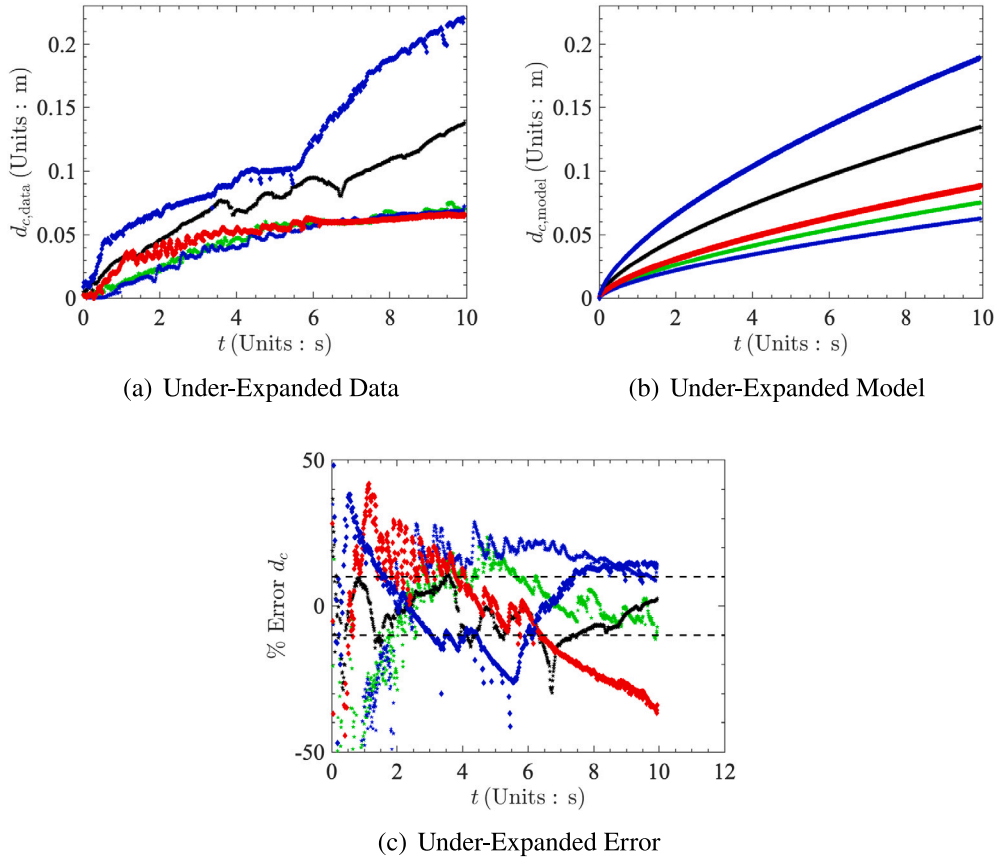


Fig. 10. Comparisons of crater depth (a) data, (b) model, and (c) error results for Under-Expanded jets. All experimental data is from [15,20,22,43,81]. A summary of conditions can be found in Appendix B. Experiments for under-expanded analysis include R5, R11, R16, R10, and R17.

CRediT authorship contribution statement

Gregory S. Shallcross: Writing – review & editing, Writing – original draft, Validation, Methodology, Investigation, Formal analysis, Conceptualization. **Jason Rabinovitch:** Writing – review & editing, Writing – original draft, Supervision, Methodology, Investigation.

Declaration of competing interest

The authors declare that they have no known competing financial interests or personal relationships that could have appeared to influence the work reported in this paper.

Acknowledgments

This research was carried out at the Jet Propulsion Laboratory, California Institute of Technology, under a contract with the National Aeronautics and Space Administration, United States [80NM0018D0004]. It is acknowledged that the compressible data was collected through the plume-surface interaction Project [80NSSC19K0488] as a part of the NASA Space Technology Mission Directorate's Game Changing Development Program. G.S. would also like to acknowledge Wesley Chambers and Ashley Korzun for providing the compressible data and participating in discussions related to analysis. In addition, G.S. would like to acknowledge Eric Slimko, Josette Bellan, Eugene Bonfiglio, Ioannis Mikellides, Ram Jonnalagada, Matthew Devost, Elizabeth Jens, and Arturo Casillas for discussions related to plume-surface interactions throughout the course of this work.

Appendix A. Discussion of energy exchange and hypersonic similarity

For literature involving plume-surface interactions, there is common reference to the hypersonic parameter as having some form of, $\sim \gamma(\gamma - 1)\text{Ma}^2$ [12,13,56]. Here, γ is the ratio of specific heat and Ma is the Mach number. While this expression is regularly referenced, the origin of the expression and assumptions associated with its use are not always clear. For the purposes of this work, the expression is derived and discussed. The process starts with the ideal gas law equation of state,

$$P = (\gamma - 1) \left(\rho E - \frac{1}{2} \rho u^2 \right), \quad (\text{A.1})$$

where P is pressure, ρ is density, E is total energy, and u is the far-field velocity. Here, one must assume a calorically perfect gas in the absence of chemical reactions. In addition, the corresponding definition for the internal energy, e , which takes the following form,

$$e = \frac{1}{(\gamma - 1) \rho} \frac{P}{\rho}. \quad (\text{A.2})$$

By definition, this expression can be found by taking the ratio of the kinetic energy and internal energy of the system given by,

$$k_{\text{hyper}} = \frac{\text{Kinetic Energy}}{\text{Internal Energy}} = \frac{\frac{1}{2} u^2}{e} = \frac{\frac{1}{2} u^2}{\frac{P}{\rho(\gamma - 1)}} \quad (\text{A.3})$$

where by definition, the speed of sound is given by $a = \sqrt{\gamma P / \rho}$. Subbing in the definition for the speed of sound,

$$k_{\text{hyper}} = \frac{1}{2} \frac{\gamma}{a^2} (\gamma - 1) u^2 = \frac{1}{2} \gamma (\gamma - 1) \text{Ma}^2, \quad (\text{A.4})$$

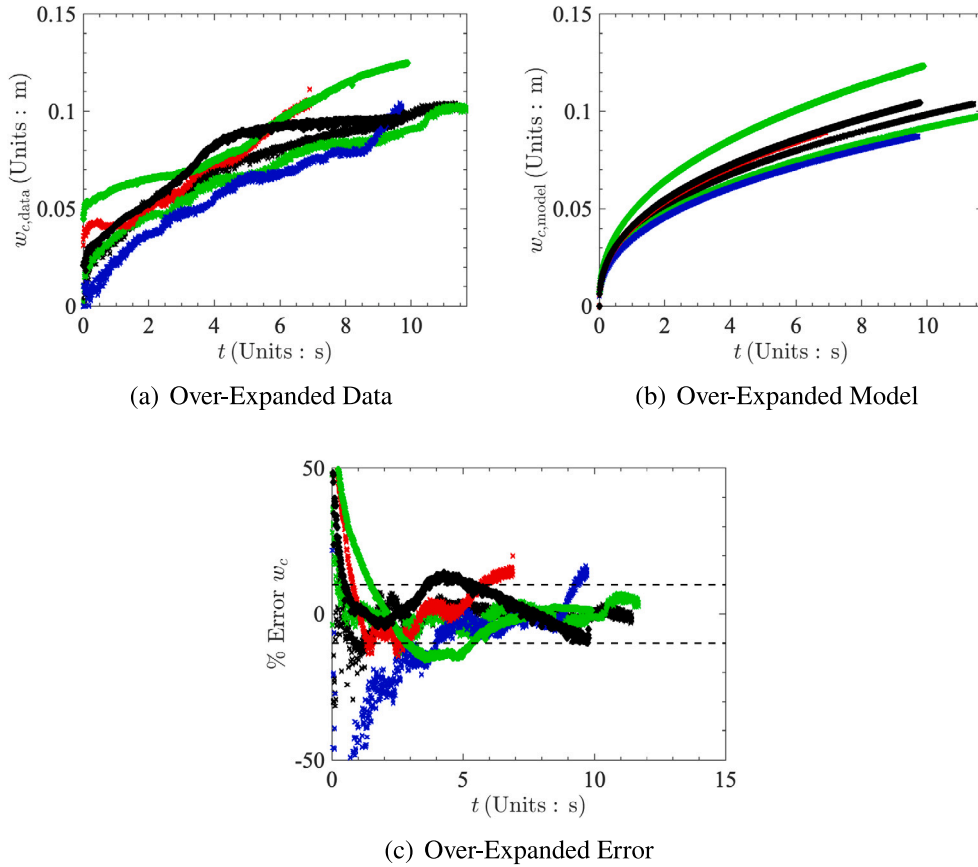


Fig. 11. Comparisons of crater width (a) data, (b) model, and (c) error results for Over-Expanded jets. All experimental data is from [15,20,22,43,81]. A summary of conditions can be found in Appendix B. Experiments for over-expanded analysis include R141, R127, R13, R8, R7, and R15.

with $Ma = u/a$.

Note that it is common for individuals to drop the leading $1/2$ factor, typical to in non-dimensional modeling and is second order to the square variation in Mach. That being said, this should not be used to describe or scale between regimes and behaviors or shock structures, but rather as a reference for the relative transition of energy between states. As described in Chernyi [92], this is used as a means to describe the transfer of kinetic energy to internal energy for high speed flow systems. When a particle, moving at a speed u , is slowed down to a stationary state, the exchange of energy from kinetic to potential energy goes as $\frac{1}{2}\gamma(\gamma - 1)Ma^2$. Thus, temperature will dramatically increase with large changes in velocity. This also supports the challenges for hypersonic flow characterization in that small relative changes in velocity can lead to large change changes in thermodynamic properties of the system.

For the traditional form of the hypersonic similarity parameter, start from the perturbation equations. These equations are a result of small perturbation theory and describe the transition between subsonic, transonic, and supersonic flow are; whereby one can describe the effect of small oscillations in flow on the energy of the system [93]. One step to derive these equations involves neglecting terms that account for correlations in fluctuations. As the velocity in the system increases, correlations in fluctuations grow and these terms are longer negligible. For very large Mach number, the Mach angle, μ , from the flow approaches the maximum deflection angle, θ , of the body. Using the small angle approximation, this means that, $\mu = \sin(\mu) = 1/Ma$ which is valid for $Ma\theta \geq 1$. The expression, $Ma\theta$, is commonly called the hypersonic similarity parameter and is typically used to treat for shock formation and similarity for flow-structure interactions.

Appendix B. A summary of experimental data and fitting conditions

In this section a summary of operating conditions is provided for a series of available experimental data for jet impingement on granular surfaces. This consists of data from Metzger et al. [20], LaMarche and Curtis [15], Korzun et al. [43] and Stubbs et al. [22,81]. For the data from Korzun et al. [43], the exit conditions were calculated using isentropic flow equations, results are found in Tables B.5 and B.6. Other compressible experiments, see Stubbs et al. [22,81], involved a sonic straight-pipe nozzle and the Fanno flow equations were used to estimate exit conditions. See Table B.7 and Table B.8 for all other appropriate operating conditions. For particle properties the mean particle diameter and bulk densities are reported. For literature that did not report bulk density, a particle packing fraction of 0.63 was assumed.

Appendix C. Comments on cohesion/adhesion modeling for granular media

Non-dimensional cohesion/adhesion modeling effects are typically defined by a modified Bond number [94] which is a ratio between the gravitational and adhesive forces (F_{ad}) on particles,

$$Bo = \frac{F_{ad}}{\frac{4}{3}\pi g R^{*3} \rho_p}. \quad (C.1)$$

Here, g is gravitational acceleration, R^* is the effective particle radius for two particles in contact given by $R^* = 2R_1R_2/(R_1 + R_2)$, and

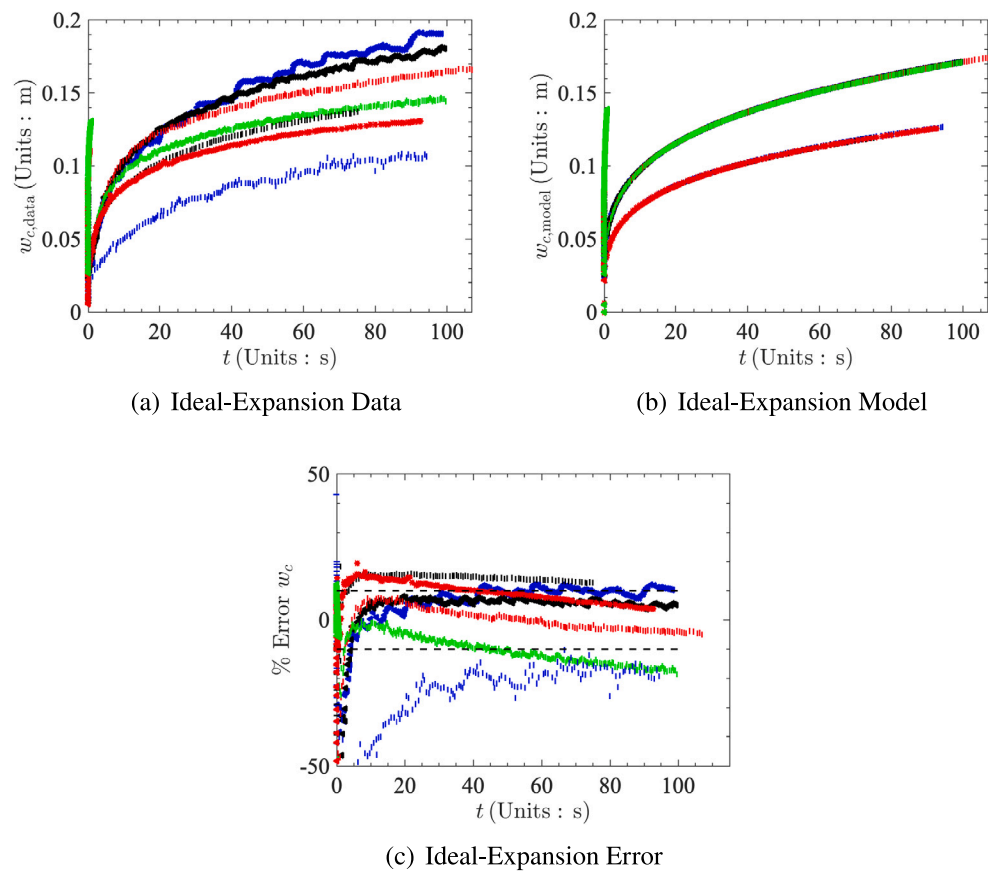


Fig. 12. Comparisons of crater width (a) data, (b) model, and (c) error results for Ideal-Expansion jets. All experimental data is from [15,20,22,43,81] A summary of conditions can be found in Appendix B. Experiments for expanded analysis include M1, M2, M3, M4, L1, L2, L3, B1, B2, B3, and B4.

Table B.5
Analysis cases for the PFGT1 and operating conditions [43]. See B.6 for the corresponding exit conditions for different flow rates.

| Case | Granular material | \dot{m} (g/s) | h/d_{jet} | P_{atm} (Pa) | Ratio | Symbol | ρ_{bulk} (kg/m ³) | \bar{d}_p (μ m) |
|-------|-------------------|--------------------|-------------|-------------------|-------|--------|---------------------------------------|---------------------------|
| R124a | IRR | 0.32 | 3 | 2.67 | UE | ● | 1300 | 281 |
| R139 | MGB | 0.32 | 8 | 2.67 | UE | ● | 1395 | 151 |
| R125 | IRR | 0.32 | 8 | 2.67 | UE | ● | 1300 | 281 |
| R18a | MDS | 0.32 | 13 | 2.67 | UE | ● | 1592 | 151 |
| R123 | IRR | 0.32 | 3 | 4 | UE | ■ | 1300 | 281 |
| R4 | MDS | 0.32 | 4 | 7 | UE | ■ | 1592 | 151 |
| R1 | MDS | 0.32 | 10 | 7 | UE | ■ | 1592 | 151 |
| R12a | MDS | 0.32 | 10 | 7 | UE | ■ | 1592 | 151 |
| R19 | MDS | 0.32 | 13 | 26.7 | UE | ▲ | 1592 | 151 |
| R9 | MDS | 8.6 | 3 | 7 | UE | ▲ | 1592 | 151 |
| R14 | MDS | 8.6 | 10 | 7 | UE | ▲ | 1592 | 151 |
| R32 | MDS | 8.6 | 10 | 26.7 | UE | ▲ | 1592 | 151 |
| R20 | MDS | 8.6 | 13 | 26.7 | UE | ★ | 1592 | 151 |
| R11 | MDS | 8.6 | 3 | 267 | UE | ★ | 1592 | 151 |
| R5 | MDS | 8.6 | 4 | 267 | UE | ★ | 1592 | 151 |
| R16 | MDS | 8.6 | 10 | 267 | UE | ★ | 1592 | 151 |
| R10 | MDS | 8.6 | 3 | 600 | UE | ◆ | 1592 | 151 |
| R17 | MDS | 8.6 | 10 | 600 | UE | ◆ | 1592 | 151 |
| R7 | MDS | 0.32 | 3 | 267 | OE | ◆ | 1592 | 151 |
| R15 | MDS | 0.32 | 10 | 267 | OE | ◆ | 1592 | 151 |
| R8 | MDS | 0.32 | 3 | 600 | OE | × | 1592 | 151 |
| R13 | MDS | 0.32 | 10 | 600 | OE | × | 1592 | 151 |
| R127 | IRR | 0.32 | 10 | 600 | OE | × | 1300 | 281 |
| R141 | MGB | 0.32 | 10 | 600 | OE | × | 1395 | 151 |

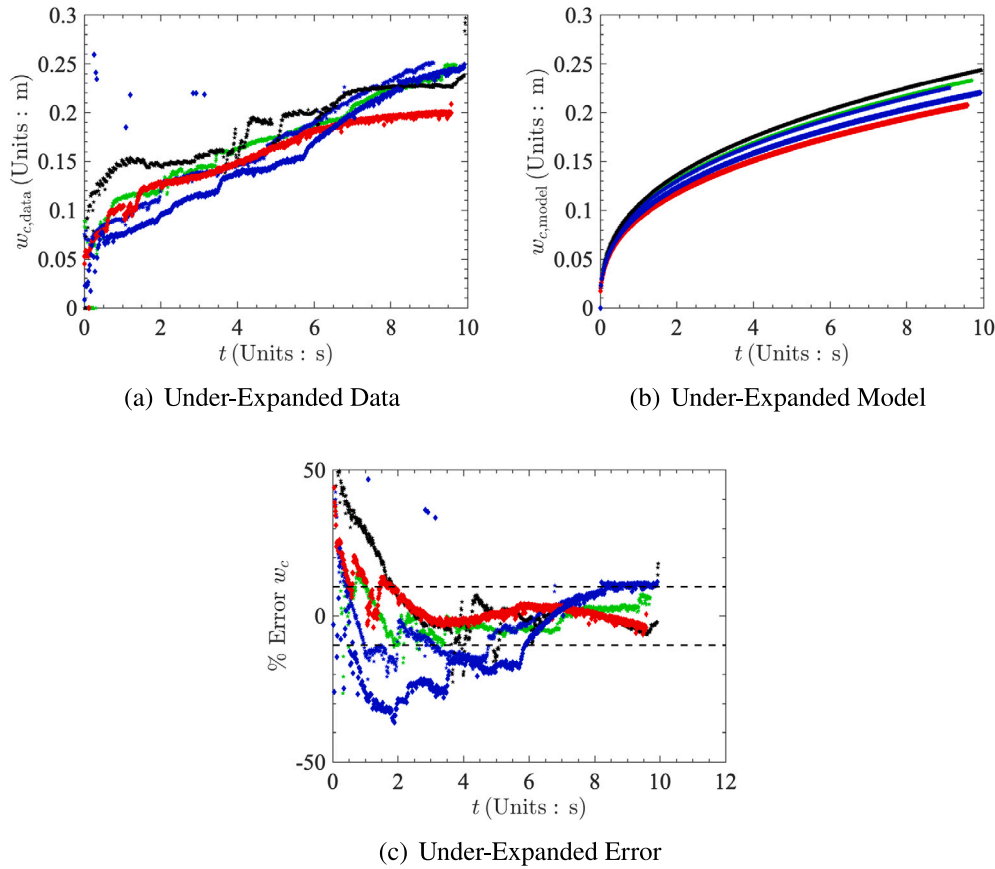


Fig. 13. Comparisons of crater width (a) data, (b) model, and (c) error results for Under-Expanded jets. All experimental data is from [15,20,22,43,81]. A summary of conditions can be found in Appendix B. Experiments for under-expanded analysis include R5, R11, R16, R10, and R17.

Table B.6

Flow operating conditions corresponding to PFGT1 [43] for cases in B.5. Calculations are based off of isentropic relations with a stagnation temperature of $T = 500$ K.

| Ma_{exit} | \dot{m} | V_{exit} | P_{exit} | ρ_{exit} |
|--------------------|-----------|-------------------|-------------------|--------------------------|
| 5.3 | 0.32 g/s | 939.7 m/s | 49.7 Pa | 0.0022 kg/m ³ |
| 5.3 | 8.6 g/s | 939.7 m/s | 1336 Pa | 0.0595 kg/m ³ |

ρ_p is the particle density. Adhesion is normally calculated with the JKR [72] or DMT [71] model for deformable larger spheres or hard small spheres respectively. These are idealized models based on smooth spherical particles and can misrepresent the actual forces for regolith adhesion [95]. Surface roughness effects can correct for these discrepancies and drastically lower adhesion forces [96]. Regardless, these effects are not always considered when calculating cohesion properties. Similar mismatches in adhesion force have been attributed to other properties like particle sphericity and lower ambient pressures [95]. In addition, specific modeling variables including surface energy, Young's modulus, and Poisson's ratio can vary from sample to sample and are critical when calculating adhesion forces [71,72,95]. Changes in local moisture content can lead to capillary effects and over estimations in adhesion forces unless otherwise characterized [74,95]. In summary, adhesive properties of granular materials can be mischaracterized for

modeling. Care must be taken if adhesion models are implemented and accurate measurements of material properties are critical for proper characterization of forces [75].

Appendix D. Uncertainty analysis for empirical fitting

In this section, uncertainty analysis is demonstrated for modeling parameters. A bootstrapping approach is applied where the population remains the same and data is sampled with replacement. Fitting parameters are repeatedly generated five thousand times per regime using the procedure from Section 3.1. The mean and standard deviations of fitted parameters are shown for over-, ideal-, and under-expanded jet conditions in Tables D.9 and D.10 for depth and width respectively. The near-vacuum conditions were omitted from this analysis due to data limitations to properly characterize height dependent time scaling $\alpha_{1,t}$, highlighted in Section 4.3.

The gravitational term, $\alpha_{7,Fr}$, was held constant and therefore has zero variation between fits. Under all regimes, $\alpha_{1,t}$ has consistently low standard deviation. For all other fitting parameters, cases with more experimental conditions and different data sources, such as the ideal-expansion data, resulted in lower standard deviations. In contrast, there is limited data for under-expanded conditions where variation in operating conditions is limited. This means unique fits are not possible, leading to larger errors in fitted parameters. It is expected that fitting errors will decrease as more data becomes available from a wide range of operating conditions.

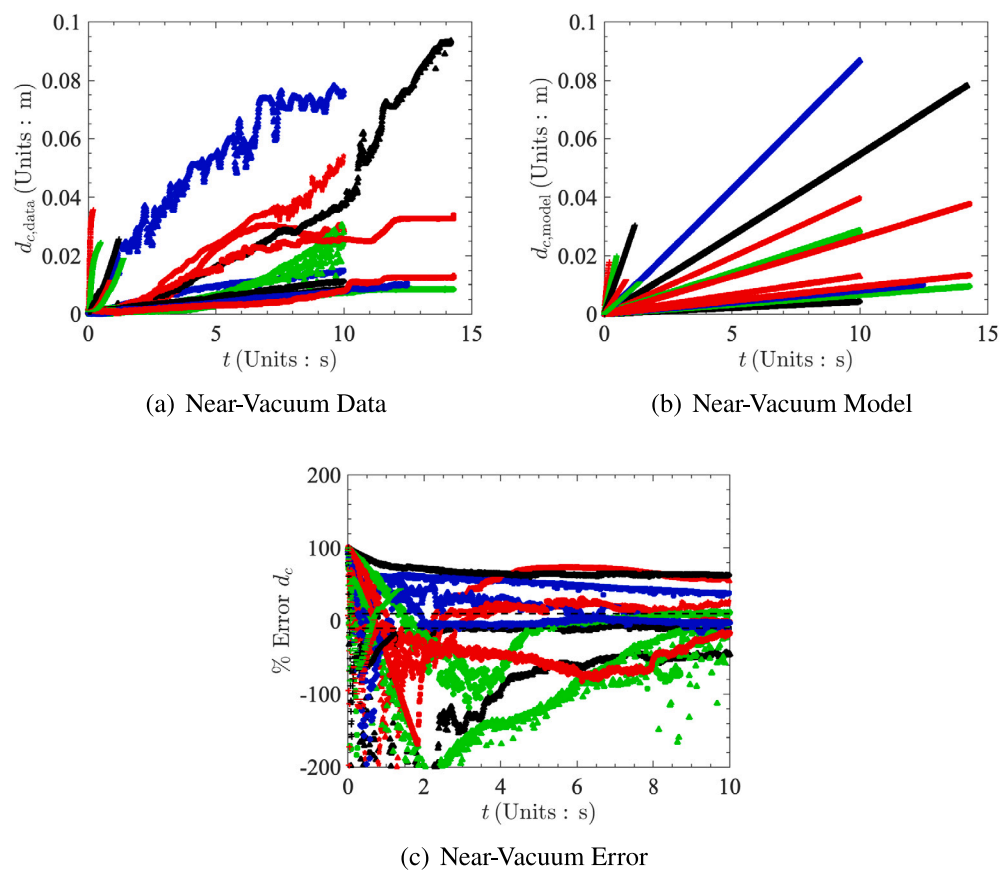


Fig. 14. Comparison of depth (a) data, (b) model, and (c) error for Near-Vacuum impingement. All experimental data is from [15,20,22,43,81]. A summary of conditions can be found in Appendix B. Near-vacuum under-expanded data includes R1, R4, R12a, R19, R32, R20, R14, R9, R123, R18a, R125, R139, R124a, A1, A2, A3, A4, and A5.

Table B.7
Analysis cases for sonic nozzle test cases and operating conditions. Cases A1–A5 are from Stubbs et al. [81] and B1–B4 are from Stubbs et al. [22].

| Case | Granular material | V_{exit} (m/s) | P_{exit} (kPa) | ρ_{exit} (kg/m ³) | h/d_{jet} | P_{atm} | Ratio | Symbol | ρ_{bulk} (kg/m ³) | \bar{d}_p (μm) |
|------|-------------------|-------------------------|-------------------------|---|--------------------|------------------|-------|--------|---|------------------|
| A1 | Sand | 320 | 103 | 1.41 | 4.6 | 33 Pa | UE | + | 1650 | 725 |
| A2 | Sand | 320 | 103 | 1.41 | 9.3 | 33 Pa | UE | + | 1650 | 725 |
| A3 | Sand | 320 | 103 | 1.41 | 13.9 | 33 Pa | UE | + | 1650 | 725 |
| A4 | Sand | 320 | 103 | 1.41 | 23.2 | 33 Pa | UE | + | 1650 | 725 |
| A5 | Sand | 320 | 103 | 1.41 | 37.1 | 33 Pa | UE | + | 1650 | 725 |
| B1 | Sand | 312 | 110 | 1.56 | 25 | 101.3 kPa | IE | — | 1650 | 725 |
| B2 | Sand | 312 | 110 | 1.56 | 40 | 101.3 kPa | IE | — | 1650 | 725 |
| B3 | Sand | 312 | 110 | 1.56 | 55 | 101.3 kPa | IE | ◀ | 1650 | 725 |
| B4 | Sand | 312 | 110 | 1.56 | 70 | 101.3 kPa | IE | ◀ | 1650 | 725 |

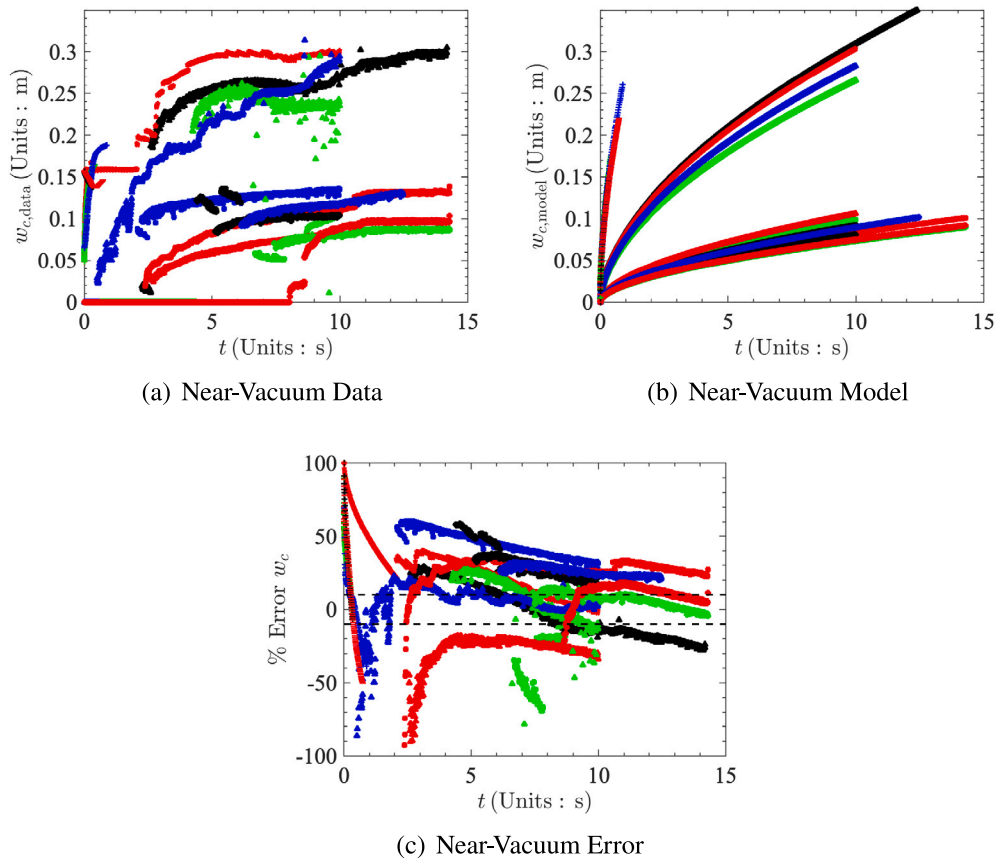


Fig. 15. Comparison of width (a) data, (b) model, and (c) error for Near-Vacuum impingement. All experimental data is from [15,20,22,43,81]. A summary of conditions can be found in Appendix B. Near-vacuum under-expanded data includes R1, R4, R12a, R19, R32, R20, R14, R9, R123, R18a, R125, R139, R124a, A1, A2, A3, A4, and A5.

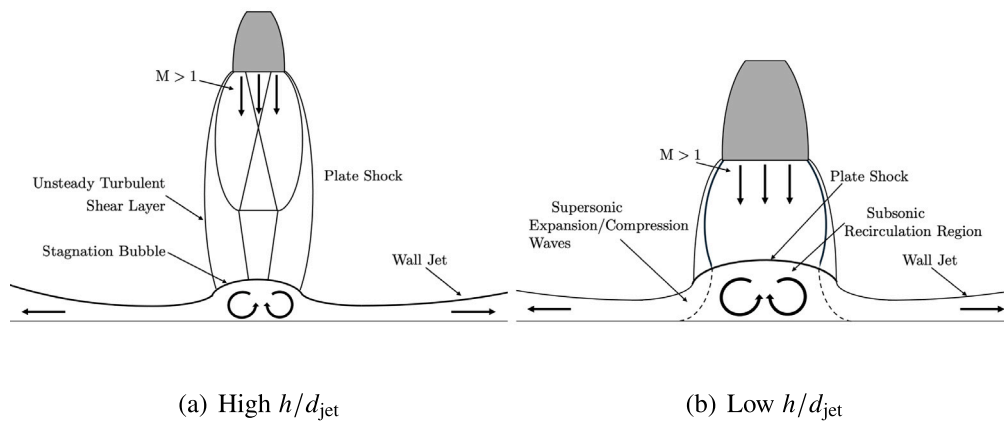


Fig. 16. Plume-surface interactions for under-expanded jet impingement for (a) high and (b) low h/d_{jet} .

Table B.8

Analysis cases for low speed flow test cases and operating conditions. Cases M1–M4 are from Metzger et al. [20] and L1–L6 are from LaMarche and Curtis [15].

| Case | Granular material | V_{exit} (m/s) | P_{exit} (kPa) | ρ_{exit} (kg/m ³) | h/d_{jet} | P_{atm} | Ratio | Symbol | ρ_{bulk} (kg/m ³) | \bar{d}_p (μm) |
|------|-------------------|----------------------------|----------------------------|--|--------------------|------------------|-------|--------|--|----------------------------------|
| M1 | Sand | 34 | 101.3 | 1.29 | 8.02 | 101.3 kPa | E | ◀ | 1700 | 240 |
| M2 | Sand | 34 | 101.3 | 1.29 | 8.02 | 101.3 kPa | E | ◀ | 1700 | 290 |
| M3 | Sand | 34 | 101.3 | 1.29 | 8.02 | 101.3 kPa | E | | 1700 | 375 |
| M4 | Sand | 34 | 101.3 | 1.29 | 8.02 | 101.3 kPa | E | | 1700 | 550 |
| L1 | Glass | 20.9 | 101.3 | 1.29 | 6.49 | 101.3 kPa | E | | 1575 | 46 |
| L2 | Glass | 20.9 | 101.3 | 1.29 | 6.49 | 101.3 kPa | E | | 1575 | 181 |
| L3 | Glass | 20.9 | 101.3 | 1.29 | 6.49 | 101.3 kPa | E | * | 1575 | 250 |
| L4 | Glass | 20.9 | 101.3 | 1.29 | 6.49 | 101.3 kPa | E | * | 1575 | 275 |
| L5 | Polystyrene | 20.9 | 101.3 | 1.29 | 6.49 | 101.3 kPa | E | * | 667 | 275 |
| L6 | Steel | 20.9 | 101.3 | 1.29 | 6.49 | 101.3 kPa | E | * | 4914 | 275 |

Table D.9

Mean and standard deviation of fitted coefficients for depth for 5000 repeated fits using bootstrapping.

| Jet expansion ratio | C_a | $\alpha_{1,i}$ | α_{2,d_p} | $\alpha_{3,\rho_{\text{bulk}}}$ | $\alpha_{4,h}$ | $\alpha_{5,\text{Re}}$ | $\alpha_{6,\text{PR}}$ | $\alpha_{8,\rho_{\text{atm}}}$ |
|---------------------|---------|----------------|------------------|---------------------------------|----------------|------------------------|------------------------|--------------------------------|
| Over, μ | 2.48 | 0.36 | 0.83 | 4.09 | −0.41 | −5.05 | 2.59 | 2.73 |
| σ | 5.52 | 1.07e−6 | 1.36e−5 | 5.15e−5 | 9.88e−7 | 0.31 | 1.81 | 1.81 |
| Ideal, μ | 0.10 | 0.19 | −0.068 | −0.69 | −0.81 | 1.25 | − | −7.13 |
| σ | 5.94e−8 | 8.15e−9 | 3.64e−8 | 6.26e−8 | 2.53e−7 | 1.13e−7 | − | 1.28e−6 |
| Under, μ | 41.09 | 0.66 | 0.57 | −0.062 | 0.63 | 0.0067 | 0.17 | 0.25 |
| σ | 26.01 | 1.70e−6 | 2.42 | 2.10 | 3.32e−7 | 1.86 | 1.96 | 1.96 |

Table D.10

Mean and standard deviation of fitted coefficients for width for 5000 repeated fits using bootstrapping.

| Jet expansion ratio | C_a | $\alpha_{1,i}$ | α_{2,d_p} | $\alpha_{3,\rho_{\text{bulk}}}$ | $\alpha_{4,h}$ | $\alpha_{5,\text{Re}}$ | $\alpha_{6,\text{PR}}$ | $\alpha_{8,\rho_{\text{atm}}}$ |
|---------------------|-------|----------------|------------------|---------------------------------|----------------|------------------------|------------------------|--------------------------------|
| Over, μ | 18.83 | 0.41 | −0.21 | −0.82 | −0.14 | 0.82 | −0.19 | −0.41 |
| σ | 12.52 | 1.09e−6 | 4.43e−6 | 2.23e−5 | 5.87e−7 | 0.46 | 1.42 | 1.42 |
| Ideal, μ | 14.48 | 0.24 | −0.002 | −0.053 | 0.0091 | 0.18 | − | −4.93 |
| σ | 17.44 | 7.78e−7 | 2.85e−6 | 0.767 | 2.62e−5 | 0.084 | − | 1.45 |
| Under, μ | 5.05 | 0.36 | 0.32 | 0.037 | 0.039 | −0.0038 | 0.19 | 0.063 |
| σ | 3.48 | 1.10e−6 | 1.80 | 1.31 | 1.63e−7 | 1.12 | 1.40 | 1.40 |

References

- [1] M. Mehta, Plume-Surface Interactions due to Spacecraft Landings and The Discovery of Water on Mars (Ph.D. thesis), University of Michigan, 2010.
- [2] G. Shallcross, Modeling Particle-Laden Compressible Flows with an Application to Plume-Surface Interactions (Ph.D. thesis), University of Michigan, 2021.
- [3] J. Cloud, R. Leuschner, T. Van Horne, Surveyor Spacecraft System-Surveyor 3 Flight Performance Final Report, Technical Report, 1967.
- [4] C. Immer, P. Metzger, P.E. Hintze, A. Nick, R. Horan, Apollo 12 lunar module exhaust plume impingement on lunar Surveyor III, *Icarus* 211 (2) (2011) 1089–1102.
- [5] C. Immer, J. Lane, P. Metzger, S. Clements, Apollo video photogrammetry estimation of plume impingement effects, *Icarus* 214 (1) (2011) 46–52.
- [6] A. Bajpai, A. Bhateja, R. Kumar, Plume-surface interaction during lunar landing using a two-way coupled DSMC-DEM approach, *Phys. Rev. Fluids* 9 (2) (2024) 024306.
- [7] P.-H. Yeh, K.-A. Chang, J. Henriksen, B. Edge, P. Chang, A. Silver, A. Vargas, Large-scale laboratory experiment on erosion of sand beds by moving circular vertical jets, *Ocean Eng.* 36 (3–4) (2009) 248–255.
- [8] J. Herauld, G. Facchini, M. Le Bars, Erosion of a sharp density interface by a turbulent jet at moderate Froude and Reynolds numbers, *J. Fluid Mech.* 838 (2018) 631–657.
- [9] K. Balakrishnan, J. Bellan, Fluid density effects in supersonic jet-induced cratering in a granular bed on a planetary body having an atmosphere in the continuum regime, *J. Fluid Mech.* 915 (2021) A29.
- [10] J. Capecelatro, Modeling high-speed gas-particle flows relevant to spacecraft landings, *Int. J. Multiph. Flow* 150 (2022) 104008.
- [11] K. Balakrishnan, J. Bellan, Added-mass and pseudo-turbulent kinetic energy effects on ejecta during jet-induced cratering in a soil, *AIAA J.* 61 (3) (2023) 973–990.
- [12] L. Roberts, The Action of a Hypersonic Jet on a Dust Layer, Technical Report, 1963.
- [13] R.E. Hutton, Comparison of Soil Erosion Theory with Scaled LM Jet Erosion Tests, Technical Report, 1968.
- [14] P.T. Metzger, J.E. Lane, C.D. Immer, J.N. Gamsky, W. Hauslein, X. Li, R.C. Latta III, C. Donaue, Scaling of erosion rate in subsonic jet experiments and Apollo lunar module landings, in: *Earth and Space 2010: Engineering, Science, Construction, and Operations in Challenging Environments*, 2010, pp. 191–207.
- [15] C.Q. LaMarche, J.S. Curtis, Cratering of a particle bed by a subsonic turbulent jet: Effect of particle shape, size and density, *Chem. Eng. Sci.* 138 (2015) 432–445.
- [16] C.J. Cuesta, J. Davies, K. Worrall, A. Cammarano, H. Zare-Behtash, Plume-surface interactions: A review of experimental work, *Acta Astronaut.* 226 (2025) 892–912.
- [17] G. Romine, T. Reisert, J. Gliozzi, Site Alteration Effects from Rocket Exhaust Impingement During a Simulated Viking Mars Landing. Part 1: Nozzle Development and Physical Site Alternation, Technical Report, NASA, 1973.
- [18] P.T. Metzger, C.D. Immer, C.M. Donahue, B.T. Vu, R.C. Latta III, M. Deyo-Svendsen, Jet-induced cratering of a granular surface with application to lunar spaceports, *J. Aerosp. Eng.* 22 (1) (2009) 24–32.
- [19] M. Mehta, N.O. Renno, J. Marshall, M.R. Grover, A. Sengupta, N.A. Rusche, J.F. Kok, R.E. Arvidson, W.J. Markiewicz, M.T. Lemmon, et al., Explosive erosion during the Phoenix landing exposes subsurface water on Mars, *Icarus* 211 (1) (2011) 172–194.
- [20] P.T. Metzger, R.C. Latta III, J.M. Schuler, C.D. Immer, Craters formed in granular beds by impinging jets of gas, in: *AIP Conference Proceedings*, vol. 1145, American Institute of Physics, 2009, pp. 767–770, 1.
- [21] D. Stubbs, L. Silwal, B.S. Thurow, M. Hirabayashi, V. Raghav, D. Scarborough, Non-intrusive, 3D optical measurements of crater formation due to plume-surface interactions, in: *AIAA Scitech 2021 Forum*, 2021, p. 0831.

- [22] D.C. Stubbs, L. Silwal, B.S. Thurow, M. Hirabayashi, V. Raghav, D.E. Scarborough, Three-dimensional measurement of the crater formation during plume–surface interactions using stereo-photogrammetry, *AIAA J.* 60 (3) (2022) 1316–1331.
- [23] W.S. Cameron, E.J. Mantel, E.R. Miller, Catalog of Lunar Mission Data, vol. 77, National Space Science Data Center, 1977, 2.
- [24] N.S. Land, L.V. Clark, Experimental Investigation of Jet Impingement on Surfaces of Fine Particles in a Vacuum Environment, National Aeronautics and Space Administration, 1965.
- [25] J. Alexander, W. Roberds, R. Scott, Soil Erosion by Landing Rockets Final Report, Technical Report, 1966.
- [26] J.E. Lane, P.T. Metzger, Estimation of Apollo lunar dust transport using optical extinction measurements, *Acta Geophys.* 63 (2015) 568–599.
- [27] L.V. Clark, Effect of Retrorocket Cant Angle on Ground Erosion-A Scaled Viking Study, Technical Report, NASA, 1970.
- [28] R. Husted, I.D. Smith, P. Fennessey, Site Alteration Effects from Rocket Exhaust Impingement During a Simulated Viking Mars Landing. Part 2: Chemical and Biological Site Alteration, Technical Report, NASA, 1977.
- [29] N.A. Holmberg, Viking’75 Spacecraft Design and Test Summary, vol. 1027, National Aeronautics and Space Administration, Scientific and Technical Information Branch, 1980.
- [30] R. Hutton, H. Moore, R. Scott, R. Shorthill, C. Spitzer, Surface erosion caused on Mars from Viking descent engine plume, *Moon the Planets* 23 (1980) 293–305.
- [31] M.P. Golombek, The Mars Pathfinder mission, *J. Geophys. Res.: Planets* 102 (E2) (1997) 3953–3965.
- [32] J.A. Crisp, M. Adler, J.R. Matijevic, S.W. Squyres, R.E. Arvidson, D.M. Kass, Mars Exploration Rover mission, *J. Geophys. Res.: Planets* 108 (E12) (2003).
- [33] P. Smith, L. Tamppari, R. Arvidson, D. Bass, D. Blaney, W. Boynton, A. Carswell, D. Catling, B. Clark, T. Duck, et al., Introduction to special section on the Phoenix mission: Landing site characterization experiments, mission overviews, and expected science, 2008.
- [34] A. Witkowski, M. Kandis, D. Kipp, D. Buecher, Mars InSight parachute system performance, in: *AIAA Aviation 2019 Forum*, 2019, p. 3481.
- [35] A.M. Korzun, R.W. Maddock, M. Schoenenberger, K.T. Edquist, C.H. Zumwalt, C.D. Karlgaard, Aerodynamic performance of the 2018 InSight Mars lander, in: *AIAA Scitech 2020 Forum*, 2020, p. 1272.
- [36] R. Prakash, P.D. Burkhart, A. Chen, K.A. Comeaux, C.S. Guernsey, D.M. Kipp, L.V. Lorenzoni, G.F. Mendeck, R.W. Powell, T.P. Rivellini, et al., Mars Science Laboratory entry, descent, and landing system overview, in: *2008 IEEE Aerospace Conference*, IEEE, 2008, pp. 1–18.
- [37] A. Nelesen, C. Sackier, I. Clark, P. Brugarolas, G. Villar, A. Chen, A. Stehura, R. Otero, E. Stille, D. Way, et al., Mars 2020 entry, descent, and landing system overview, in: *2019 IEEE Aerospace Conference*, IEEE, 2019, pp. 1–20.
- [38] A. Steltzner, D. Kipp, A. Chen, D. Burkhart, C. Guernsey, G. Mendeck, R. Mitchell, R. Powell, T. Rivellini, M. San Martin, et al., Mars Science Laboratory entry, descent, and landing system, in: *2006 IEEE Aerospace Conference*, IEEE, 2006, pp. 15–pp.
- [39] M.S. Manginelli, M. Mehta, O.H. Thomas, Flight reconstruction of plume-induced site alteration from InSight, *J. Spacecr. Rockets* 58 (3) (2021) 879–893.
- [40] J. Vizcaino, M. Mehta, Quantification of plume-soil interaction and excavation due to the Mars Science Laboratory sky crane descent phase, in: *8th Symposium on Space Resource Utilization*, 2015, p. 1649.
- [41] J. Rabinovitch, S.A. Santana, C.D. Karlgaard, E.T. Jens, K.M. Stack, D.M. Turner, W.A. Chambers, M. Mehta, A.M. Korzun, Observed high-altitude surface erosion during the Mars Science Laboratory and Mars 2020 landings, *J. Spacecr. Rockets* 61 (1) (2024) 313–318.
- [42] S.D. Guleria, D.V. Patil, Experimental investigations of crater formation on granular bed subjected to an air-jet impingement, *Phys. Fluids* 32 (5) (2020).
- [43] A.M. Korzun, C.J. Eberhart, J. West, P. Liever, A. Weaver, J. Mantovani, A. Langton, B. Kemmerer, A. Atkins, Design of a subscale, inert gas test for plume-surface interactions in a reduced pressure environment, in: *AIAA Scitech 2022 Forum*, 2022, p. 1808.
- [44] M.X. Diaz-Lopez, M. Gorman, J.S. Rubio, R. Ni, Plume-surface interaction physics focused ground test 1: Diagnostics and preliminary results, in: *AIAA Scitech 2022 Forum*, 2022, p. 1810.
- [45] J.S. Rubio, M. Gorman, M.X. Diaz-Lopez, R. Ni, Plume-surface interaction physics focused ground test 1: Setup and preliminary results, in: *AIAA Scitech 2022 Forum*, 2022, p. 1809.
- [46] T. Crane, D. Stubbs, B.S. Thurow, V. Raghav, D. Scarborough, Three-dimensional crater formation measurements during plume-surface interaction in a reduced gravity environment using a drop tower, in: *AIAA Scitech 2024 Forum*, 2024, p. 2525.
- [47] L. Silwal, V.N. Bhargav, D.C. Stubbs, B.K. Fulone, B.S. Thurow, D.E. Scarborough, V. Raghav, Ejecta behavior during plume-surface interactions under rarefied atmospheric conditions, *Acta Astronaut.* 218 (2024) 35–46.
- [48] R. Maddock, FY22 CLPS PSI mini-suite annual review presentation, in: *GCD FY22 Annual Review*, 2022.
- [49] R. Maddock, PSI flight measurement development status, in: *Gateway Dust Mitigation Working Group*, 2024.
- [50] K. Balakrishnan, J. Bellan, High-fidelity modeling and numerical simulation of cratering induced by the interaction of a supersonic jet with a granular bed of solid particles, *Int. J. Multiph. Flow* 99 (2018) 1–29.
- [51] G.S. Shallcross, R.O. Fox, J. Capece, A volume-filtered description of compressible particle-laden flows, *Int. J. Multiph. Flow* 122 (2020) 103138.
- [52] K. Balakrishnan, J. Bellan, Ejecta from granular-medium cratering by a supersonic jet entering a continuum atmosphere, *AIAA J.* 59 (10) (2021) 3799–3814.
- [53] P. Liever, A. Tosh, R. Arslanbekov, S. Habchi, Modeling of rocket plume impingement flow and debris transport in lunar environment, in: *50th AIAA Aerospace Sciences Meeting Including the New Horizons Forum and Aerospace Exposition*, 2012, p. 800.
- [54] A.B. Morris, Simulation of Rocket Plume Impingement and Dust Dispersal on the Lunar Surface (Ph.D. thesis), The University of Texas at Austin, 2012.
- [55] W.A. Hoey, M.G. Martin, J.M. Alred, C.E. Soares, M.T. Ababneh, Analyses of Blue Origin Blue Moon lunar landing descent engine plume effects, 2023.
- [56] P.T. Metzger, J.E. Lane, C.D. Immer, Modification of Roberts’ theory for rocket exhaust plumes eroding lunar soil, in: *Earth & Space 2008: Engineering, Science, Construction, and Operations in Challenging Environments*, 2008, pp. 1–8.
- [57] P.T. Metzger, Erosion rate of lunar soil under a landing rocket, part 1: Identifying the rate-limiting physics, *Icarus* 417 (2024) 116136.
- [58] P.T. Metzger, Erosion rate of lunar soil under a landing rocket, part 2: Benchmarking and predictions, *Icarus* 417 (2024) 116135.
- [59] B. Dotson, A. St John, R. Hall, D. Sapkota, D. Britt, P. Metzger, Understanding the effects of geotechnical properties on viscous erosion rate from plume surface interactions, *Planet. Space Sci.* 261 (2025) 106117.
- [60] A.B. Morris, D.B. Goldstein, P.L. Varghese, L.M. Trafton, Approach for modeling rocket plume impingement and dust dispersal on the Moon, *J. Spacecr. Rockets* 52 (2) (2015) 362–374.
- [61] S.K. Mishra, K.D. Prasad, Numerical evaluation of surface modifications at landing site due to spacecraft (soft) landing on the Moon, *Planet. Space Sci.* 156 (2018) 57–61.
- [62] J. You, X. Zhang, H. Zhang, C. Li, Y. Xu, Q. Yan, H. Yu, J. Liu, Y. Li, Y. Wang, et al., Analysis of plume–lunar surface interaction and soil erosion during the Chang’E-4 landing process, *Acta Astronaut.* 185 (2021) 337–351.
- [63] S.T. Shipley, E. Eloranta, J. Weinman, Measurement of rainfall rates by lidar, *J. Appl. Meteorol. Clim.* 13 (7) (1974) 800–807.
- [64] D. Rosenfeld, D.B. Wolff, D. Atlas, General probability-matched relations between radar reflectivity and rain rate, *J. Appl. Meteorol. Clim.* 32 (1) (1993) 50–72.
- [65] G.I. Taylor, The formation of a blast wave by a very intense explosion I. Theoretical discussion, *Proc. R. Soc. Lond. Ser. A* 201 (1065) (1950) 159–174.
- [66] T. Szirtes, *Applied Dimensional Analysis and Modeling*, Butterworth-Heinemann, 2007.
- [67] J.C. Gibbins, *Dimensional Analysis*, Springer Science & Business Media, 2011.
- [68] N.-E.S. Chemoul, *Dimensional Analysis and Similarity in Fluid Mechanics*, John Wiley & Sons, 2020.
- [69] R.A. Bagnold, *The Physics of Blown Sand and Desert Dunes*, Courier Corporation, 2012.
- [70] J.B. Pollack, R. Haberle, R. Greeley, J. Iversen, Estimates of the wind speeds required for particle motion on Mars, *Icarus* 29 (3) (1976) 395–417.
- [71] B.V. Derjaguin, V.M. Muller, Y.P. Toporov, Effect of contact deformations on the adhesion of particles, *J. Colloid Interface Sci.* 53 (2) (1975) 314–326.
- [72] K.L. Johnson, K. Kendall, A. Roberts, Surface energy and the contact of elastic solids, *Proc. R. Soc. Lond. Ser. A* 324 (1558) (1971) 301–313.
- [73] S. You, M.P. Wan, Modeling and experiments of the adhesion force distribution between particles and a surface, *Langmuir* 30 (23) (2014) 6808–6818.
- [74] S. You, M.P. Wan, Mathematical models for the van der Waals force and capillary force between a rough particle and surface, *Langmuir* 29 (29) (2013) 9104–9117.
- [75] G.S. Shallcross, W.A. Hoey, J.R. Anderson, C. Soares, M. Cooper, Modeling adhesion and aerodynamic removal of particles and spores from substrates, *J. Aerosol Sci.* 176 (2024) 106294.
- [76] K.A. Holsapple, K.R. Housen, Momentum transfer in asteroid impacts. I. Theory and scaling, *Icarus* 221 (2) (2012) 875–887.
- [77] J. Chen, G. Zhang, J.-H. Si, H. Shi, X. Wang, Experimental investigation of scour of sand beds by submerged circular vertical turbulent jets, *Ocean Eng.* 257 (2022) 111625.
- [78] D.C. Stubbs, L. Silwal, V.N. Bhargav, B.S. Thurow, V. Raghav, D.E. Scarborough, The effect of reduced ambient pressure on plume-surface interaction cratering dynamics, *AIAA J.* 63 (3) (2025) 1062–1077.
- [79] M.T. Gorman, J.S. Rubio, M.X. Diaz-Lopez, W.A. Chambers, A.M. Korzun, J. Rabinovitch, R. Ni, Scaling laws of plume-induced granular cratering, *PNAS Nexus* 2 (9) (2023) pgad300.
- [80] K.A. Holsapple, The scaling of impact processes in planetary sciences, *Annu. Rev. Earth Planet. Sci.* 21 (1) (1993) 333–373.
- [81] D. Stubbs, L. Silwal, V.N. Bhargav, B.S. Thurow, M. Hirabayashi, V. Raghav, D.E. Scarborough, Non-intrusive, 3-D crater formation measurements due to plume-surface interactions under sub-atmospheric pressure conditions, in: *AIAA Scitech 2023 Forum*, 2023, p. 2488.
- [82] MathWorks Inc, MATLAB, version: 9.13. 0 (R2020b), 2020.

- [83] N. Rodrigues, O. Tyrrell, P. Danehy, Fluorescence imaging of plume-surface interaction in large-scale reduced pressure environments, *Phys. Fluids* 36 (10) (2024).
- [84] N.S. Rodrigues, R.A. Burns, O.K. Tyrrell, P.M. Danehy, Wall-jet evolution during plume-surface interaction using fluorescence imaging, in: *AIAA Scitech 2025 Forum*, 2025, p. 2402.
- [85] A.R. Vick, et al., An Investigation of Highly Underexpanded Exhaust Plumes Impinging Upon a Perpendicular Flat Surface, Technical Report, 1966.
- [86] P. Sonar, H. Katsuragi, Air-jet impact craters on granular surfaces: a universal scaling, *J. Fluid Mech.* 998 (2024) A29.
- [87] R. Greeley, R. Leach, B. White, J. Iversen, J. Pollack, Threshold windspeeds for sand on Mars: Wind tunnel simulations, *Geophys. Res. Lett.* 7 (2) (1980) 121–124.
- [88] N. Rajaratnam, S. Beltaos, Erosion by impinging circular turbulent jets, *J. Hydraul. Div.* 103 (10) (1977) 1191–1205.
- [89] G. Bird, Breakdown of translational and rotational equilibrium in gaseous expansions, *AIAA J.* 8 (11) (1970) 1998–2003.
- [90] B. Henderson, The connection between sound production and jet structure of the supersonic impinging jet, *J. Acoust. Soc. Am.* 111 (2) (2002) 735–747.
- [91] B. Henderson, J. Bridges, M. Wernet, An experimental study of the oscillatory flow structure of tone-producing supersonic impinging jets, *J. Fluid Mech.* 542 (2005) 115–137.
- [92] G.G. Chernyi, *Introduction to Hypersonic Flow*, Academic Press, 2013.
- [93] H.W. Liepmann, A. Roshko, *Elements of Gasdynamics*, Courier Corporation, 2001.
- [94] A. Jarray, H. Shi, B.J. Scheper, M. Habibi, S. Luding, Cohesion-driven mixing and segregation of dry granular media, *Sci. Rep.* 9 (1) (2019) 13480.
- [95] Y. Nagaashi, T. Aoki, A.M. Nakamura, Cohesion of regolith: Measurements of meteorite powders, *Icarus* 360 (2021) 114357.
- [96] W. Cheng, P. Dunn, R. Brach, Surface roughness effects on microparticle adhesion, *J. Adhes.* 78 (11) (2002) 929–965.